The Meteoritical Society

Meteoritics & Planetary Science 50, Nr 1, 112–134 (2015)
doi: 10.1111/maps.12406

Formation of a small impact structure discovered within the Agoudal meteorite strewn field, Morocco

C. A. LORENZ[1*], M. A. IVANOVA[1], N. A. ARTEMIEVA[2,3], D. A. SADILENKO[1], H. CHENNAOUI AOUDJEHANE[4], I. A. ROSCHINA[1], A.V. KOROCHANTSEV[1], and M. HUMAYUN[5]

[1]Vernadsky Institute of Geochemistry and Analytical Chemistry, Kosygin St. 19, Moscow 119991, Russia
[2]Institute for Dynamics of Geospheres, Leninsky Prospect St. 38, Bld.1, Moscow 119334, Russia
[3]Planetary Science Institute, 1700 E. Ft. Lowell Rd., Suite 106, Tucson, Arizona 85719, USA
[4]Hassan II University Casablanca, Faculty of Sciences, GAIA Laboratory, BP 5366 Maârif, 20000 Casablanca, Morocco
[5]National High Magnetic Field Laboratory and Department of Earth, Ocean & Atmospheric Science, Florida State University, 1800 E. Paul Dirac Drive, Tallahassee, Florida 32310, USA
[*]Corresponding author. E-mail: c-lorenz@yandex.ru

(Received 05 November 2013; revision accepted 28 October 2014)

Abstract–A relic impact structure was recognized within the strewn field of the Agoudal iron meteorite. The heavily eroded structure has preserved shatter cones in a limestone basement, and remnants of autochthonous and allochthonous breccias. Fragments of iron incorporated into the allochthonous breccia have a chemical composition (Ni = 5.16 wt%, Ir = 0.019 ppm) similar to that of the Agoudal meteorite, supporting a syngenetic origin of the strewn field and the impact structure. The total recovered mass of Agoudal meteorite fragments is estimated at approximately 500 kg. The estimated size of the SE–NW-oriented strewn field is 6 × 2 km. Model calculations with minimal preatmospheric size show that a similar meteorite strewn field plus one small crater with observed shock effects could be formed by fragmentation of a meteoroid approximately 1.4 m in diameter with an impact angle of approximately 60° from the horizontal. However, the most probable is an impact of a larger, 3–4 m diameter meteoroid, resulting a strewn field with approximately 10 craters, 10–30 m in diameter each, plus numerous meteorite fragments. The calculated scattering area of meteorite shrapnel ejected from these impact craters could completely cover the observed strewn field of the Agoudal meteorite.

INTRODUCTION

Fragmentation of a meteoroid in the lower atmosphere generates a strewn field of meteorites approximated by an ellipse, oriented along the meteoroid trajectory. In the simplest case of one fragmentation event and flat horizontal target terrain, the larger masses reach the surface further downrange than the smaller masses, with the main mass of meteorite falling in the head of the scattering ellipse (Nininger 1963). The real geometry of meteorite scattering areas depends on the entry angle of the meteoroid into Earth's atmosphere, fragmentation scenario, and on the local relief of the target terrain. Entry angle of 90° produces a circular scattering area; and lower entry angles produce elongated elliptical strewn fields. The meteorite pieces formed as a result of midatmosphere fragmentation, called individual samples (or individuals), have various shapes depending on the physical–mechanical properties of the meteorite material. Typically, they are smooth, with surfaces covered by cavities (regmaglypts) formed by ablation of the meteorites in the atmosphere.

Above a certain energy threshold, some meteoroid fragments reach the surface with high enough velocity to produce impact craters and ejecta. In this case, meteorite fragments (shrapnel) ejected from these craters can be scattered around, in some cases overlapping the meteorite strewn field. The shrapnel fragments of iron meteorites have flattened shape, rugged sharp edges, and rough surface without regmaglypts. Projectile fragment

distribution around craters can also be asymmetric depending mainly on impact angle and target surface inclination (Kofman et al. 2010; D'Orazio et al. 2011; Folco et al. 2011).

During high-energy impact cratering, the meteoritic projectile is melted and/or vaporized (Melosh 1989). Thus, surviving meteorite fragments genetically linked with old, high-energy impact craters have rarely been found on Earth. However, small, geologically young craters sometimes contain remnants of well-preserved meteoritic projectile material (e.g., Folco et al. 2010; Kofman et al. 2010). Insights into how small impact craters are formed can be obtained from geological and morphological studies of these craters combined with the analysis of meteorite fragments associated with these craters (Kenkmann et al. 2009; Kofman et al. 2010; Folco et al. 2011). Experimental (e.g., Poelchau et al. 2013), and numerical (Bland and Artemieva 2006) models also help to reconstruct small impact events.

Occasionally, ancient meteorite falls are recovered. Their sample distribution can be disturbed by surface processes determined by the local relief, geology, and climate. There are 184 confirmed impact structures on Earth (Earth Impact Database, http://www.passc.net/EarthImpactDatabase/index.html). Most of the small (≤150 m) craters are associated with iron meteorites (Table 1). The main difficulty in the study of exposed small craters is the incomplete preservation of the impact structures and meteorite fragments. The preservation of small impact structures and occurrence of shock features in their target rocks depends on the age of the crater, target rock composition, energy of impact, and geomorphological conditions. Many small craters have been found in target areas comprised of quaternary sediments and soils, or partly covered by them. In these cases, shock features are poorly observed.

A small, eroded impact structure was recognized recently in the High Atlas Mountains of Morocco during exploration of the Agoudal iron meteorite strewn field (Sadilenko et al. 2013). The Agoudal iron meteorite was investigated and classified recently as a IIAB iron (Chennaoui Aoudjehane et al. 2013). The purpose of this paper was to reconstruct the fall of the Agoudal iron meteorite based on data about the distribution of meteorite fragments within the scattering area. We also discuss a possible genetic relationship between the Agoudal iron fall and the small, eroded impact structure. Our results allow constraints to be placed on parameters of the formation of the impact structure found near the Agoudal strewn field, including the orientation of the meteoroid trajectory; its preatmospheric parameters (impact velocity, angle, mass); shock pressure; and distribution, sizes, shapes, and masses of the meteorite fragments.

METHODS

Two polished thin sections of polymict breccia (approximately 4 cm^2 total area) and one polished thin section of shattered limestone from the small, eroded impact structure's main outcrop were studied by optical microscopy (Leica DMC microscope), backscattered electron (BSE) imaging, and electron probe microanalysis at the Vernadsky Institute of the Russian Academy of Sciences in Moscow and at the Smithsonian Institution, National Museum of Natural History (Washington, D.C., USA). BSE images were obtained using an FEI Nova NanoSEM 600 scanning electron microscope, equipped with a Thermo Electron energy dispersive X-ray spectrometer. The SEM was operated at 15 kV, with a beam current of 2–3 nA. Mineral chemical compositions were determined with a CAMECA SX100 at the Vernadsky Institute. Chemical analyses were performed at 15 kV accelerating voltage for silicates, oxides, and carbonates, 20 nA beam current, and 40 s counting time. Well-characterized silicates, oxides, metals, and sulfides were used as standards. Bulk chemical compositions of selected areas of thin sections were measured by acquiring approximately 7 × 7, 10 × 10, and 20 × 20 μm broad beam analyses. Matrix corrections were applied using the PAP procedure.

Approximately 20 g samples of breccia and shattered limestone from the bottom of the main outcrop were crushed and powdered in an agate mortar to obtain representative average samples for bulk-rock major and trace element determinations. Of each sample, 300 mg was used for X-ray fluorescence (XRF) analysis for Si, Al, Ti, Ca, Mg, Cr, Mn, K, Na, Fe at the Vernadsky Institute (Panalytical Axios XRF spectrometer). Exactly 100 mg of the breccia and shattered limestone samples were analyzed for measurements of trace element chemistry, mostly Ni and Co, using inductively coupled plasma–mass spectrometry (ICP-MS) at the Institute of Geology of Ore Deposits, Petrography, Mineralogy and Geochemistry (Moscow).

A polished section consisting of a fragment of the Agoudal iron meteorite and a fragment of iron metal recovered from the breccia from the eroded impact structure were investigated by laser ablation ICP-MS analysis. A 20 mm × 6 mm polished surface of the Agoudal iron meteorite with minimal weathering and a 22 mm × 13 mm polished fragment of iron embedded in the impact breccia were mounted in epoxy. Siderophile elements were determined by rastering of areas A2 (1.8 mm^2) on the Agoudal iron meteorite; and A3 + 4 (2.1 mm^2) and A5 (1.8 mm^2) on the metal from the impact breccia. Laser ablation ICP-MS analyses were performed with a New Wave UP193FX excimer laser system coupled to an Electro Scientific Industries

Table 1. Proven impact craters with diameter less than 150 m.

Name	D, m[a,b]	Age, Ka[b]	Target[c]	Impactor	Shock metamorphism effects	Estimated shock pressure	Ref.
Carancas	13.5	0.006	ncs	Stone	Not reported	<5 GPa[d]	[1]
Haviland	15	1	ncs	Stony-iron	Not reported		[9]
Dalgaranga	27	270	wcr	Stony-iron	Not reported	<2 GPa[d]	[2]
Sikhote-Alin	27	0.063	cr	Iron	Coarse shatter cones		[10]
Whitecourt	36	1.1	ncs	Iron	PDF in quartz; small-scale melting of impactor	≥5 GPa[d]	[7]
Kamil	45	5	cs	Iron	Small-scale melting of target and impactor, PDF in quartz grains, shatter cones were not reported	>20 GPa	[5]
CampoDel Cielo	50	< 4	ncs	Iron	Not reported		[8]
Sobolev	53	1	cr	Iron	Not reported		
Veevers	80	20	ncs	Iron	Not reported in target; reheating to >800 °C, shearing and plastic deformation of the impactor		[2]
Morasko	100	10	ncs	Iron	Not reported in target; plastic deformations and reheating of the impactor up to approximately 500 °C, maximum >800 °C, probably small-scale melting of the impactor		[4]
Kaalijärv	110	4	cs	Iron	Not reported in target; plastic deformations and reheating of the impactor up to 600–850 °C		[3]
Wabar	110	0.14	ncs	Iron	PDF in quartz, lechatelierite, coesite, small-scale melting of target and impactor	25–45 GPa	[6]

[a]Crater diameter.
[b]Data are obtained from the Earth Impact Database.
[c]Target rock types: ncs = nonconsolidated sediment (sands and clays); cs = consolidated sediment (sandstone, limestone); cr = crystalline, wcr = weathered crystalline.
[d]Estimation of shock pressure by occurrence of impact metamorphism features: <5 GPa—No PDF in quartz were found; shattercones cannot be present in loose or unconsolidated target rocks; <2 GPa—PDF in quartz and shattercones in target rocks are not present.
[1] Kenkmann et al. (2009); [2] Bevan et al. (1995) and Shoemaker et al. (2005); [3] Semenenko et al. (1982) and Plado (2012); [4] Dominik (1977) and Classen (1978); [5] Folco and D'Orazio (2011) and Folco et al. (2011); [6] Spencer (1933), Bunch and Cohen (1964), Chao et al. (1961), and Johnson et al. (1988); [7] Kofman et al. (2010); [8] Cassidy et al. (1965); [9] Nininger and Figgins (1933); [10] Krinov (1971).

Thermo Element XR at the Plasma Analytical Facility, Florida State University (Humayun et al. 2007; Humayun 2012). A 100 μm beam spot scanned at 25 μm s^{-1}, 50 Hz repetition rate, with 2 GW cm^{-2} fluence, was used. Standardization of the measurements is identical to that previously described (Campbell et al. 2002; Humayun 2012). Importantly, the IIAB iron meteorite North Chile (Filomena) was used as a standard for calibration of Ni, Ga, Ge, Cu, W, and Au (Wasson et al. 1989). The precision obtained on these measurements is better than 5% for most elements, except P, S, and Cr (due to heterogeneous distribution) and of Re (15–25%, due to lower count rates).

To model the flight, atmospheric entry, and breakup of the Agoudal meteorite, we used the separated fragments (SF) model (Artemieva and Shuvalov 2001; Bland and Artemieva 2006) with the following initial conditions: an iron spherical body with a density of 7800 kg m^{-3}, strength of 4.4×10^7 Pa (for 1 kg sample; Zotkin and Tsvetkov 1983), and ablation coefficient of 0.07 s^2 km^{-2} in accordance with theoretical calculations (ReVelle and Rajan 1988), and with observations of U.S.

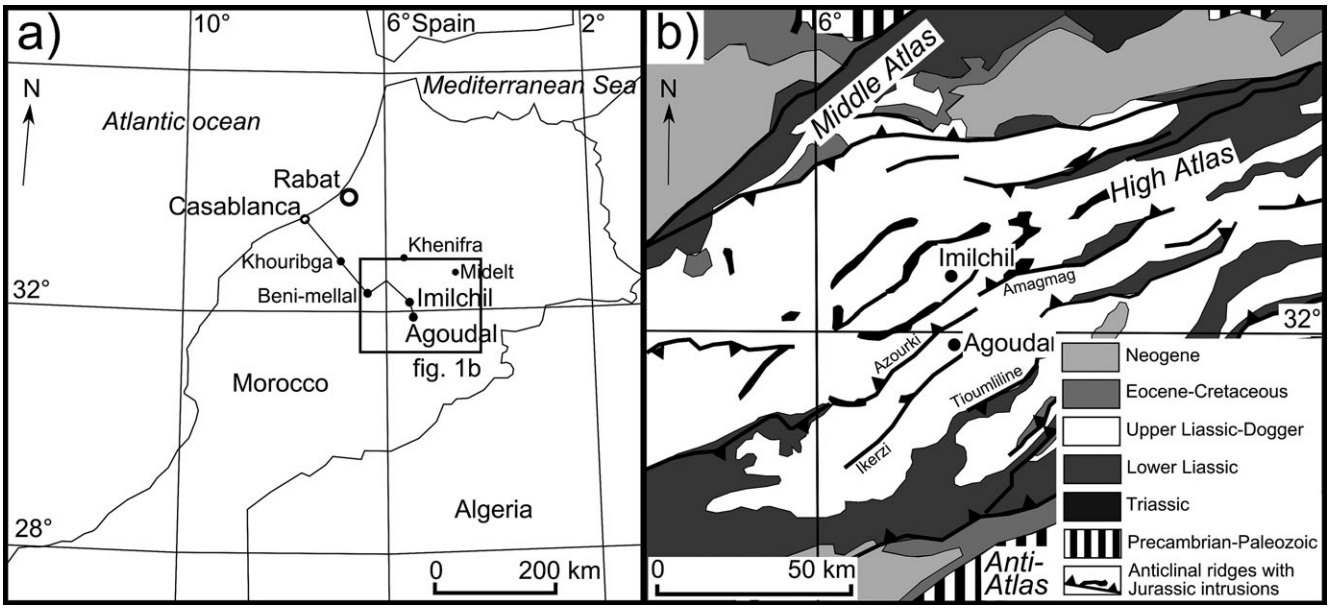

Fig. 1. a) Location map of the Agoudal site; b) simplified schematic structural map of the Agoudal site (after Michard et al. [2011] and references therein).

Prairie Network fireballs identified as irons (ReVelle and Ceplecha 1994). We also used an asteroid–Earth encounter velocity of 18 km s^{-1} (Shoemaker 1977) and atmospheric entry angles of 45° and 60°. We used the SOVA program code (Shuvalov 1999) to model impacts into slopes, transient cavity formation, and projectile/target ejecta distributions.

RESULTS

Geomorphology at the Agoudal Site

The Agoudal strewn field is located in the High Atlas Mountains of Morocco, about 20 km southeast of Imilchil city and 4 km west of the village of Agoudal (Fig. 1a). The R704 road passes across the northern part of the scattering area (Fig. 2a). The High Atlas Mountains of Morocco, representing the southernmost element of the Peri-Mediterranean Alpine belts, is a typical example of an intracontinental mountain belt (Ellero et al. 2012) (Fig. 1b). The Central High Atlas is characterized by alkaline-transitional gabbroic magmatism emplaced in the form of sills, dykes, and outpours (Fig. 1b). Marine sedimentation resumed during the Aptian. Within the mountain belt, narrow, faulted anticlinal ridges cored by Triassic argillites and magmatic rocks extend between wide open synclines (Michard et al. 2011). The area of the Agoudal site is comprised of Jurassic sedimentary rocks of the Binelouidane Marly Limestone Formation of Bajocian (Middle Dogger) age (Fig. 1b).

Most of the meteorite finds are located within a river valley (the "main valley") oriented SW to NE. The valley has an asymmetrical cross sectional profile. The north side of the valley has a steep slope that rises into a scarp-topped mountain. Near the base of the slope, finer-grained proluvial and alluvial sediments are present; above that, on the middle part of the mountainside, a poorly sorted colluvium is present. The south side of the valley is a broad slope rising into a chain of mesa-like mountains. This side of the valley is channeled by approximately south–north-oriented wadis and is covered by a layer of sediments mostly comprised of sands and clays. Measured thickness of the sediments on the flat tops of several mesas and on the lower wadi slopes is 5–20 cm, in the wadi channels approximately 50 cm, and near the wadi mouths can be more than 2 m (observed on the wall of a dry well). Thus, the territory of the meteorite strewn field has an intensively channeled relief that is a combination of slopes and temporal flows, and is an area of intensive erosion, followed by accumulation of removed material, that could bury meteorite samples to significant depth and, probably, transport them from their initial positions down toward the main river valley.

Total Recovered Mass Estimate

Initial information about possible iron meteorite finds near Agoudal village was received when two small pieces of iron (masses are unknown) collected in the Agoudal area in 2000 were sold to tourists. In September 2011, another piece of iron from Agoudal

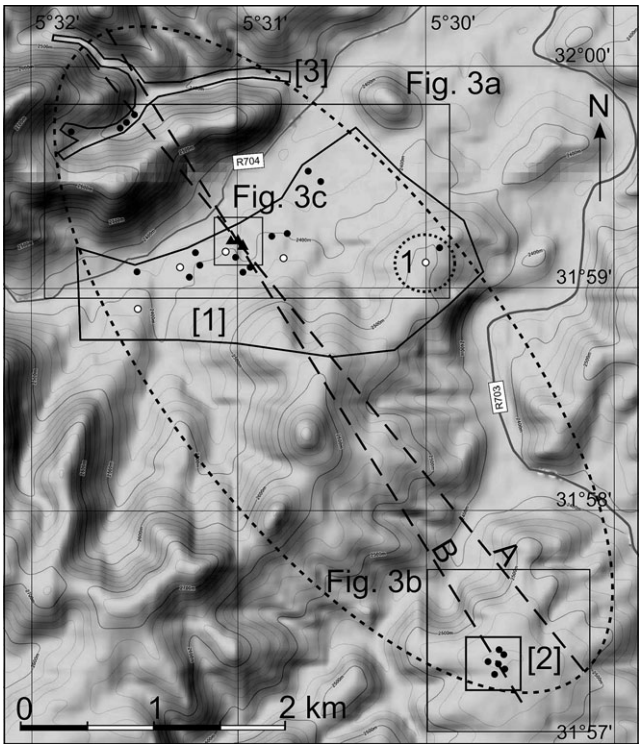

Fig. 2. Overview map of locations of the Agoudal meteorite sample finds. Black circles—finds; white circles—old pits, locations of possible undocumented finds; triangles—impactite outcrops; solid contours—areas of search by: [1] Moroccan team, 2013, Russian team, 2013–2014, main valley; [2] Moroccan team, 2013, southern finds; [3] Russian team, 2013–2014, northern valley; circle—approximate area of numerous small finds around point 1; dashed ellipse—proposed scattering area of the Agoudal meteorite; dashed lines—proposed axes of the strewn field, drawn through the impact structure and 52 kg find in the northern valley (line A) and through the impact structure and the southern cluster of finds (line B).

was sold to a dealer in Er-Rich, who recognized it as an iron meteorite (mass is unknown). In late 2012, intensive undocumented searching of the Agoudal strewn field by local residents using metal detectors resulted in the discovery of a large number of mostly small samples which were collected on the surface or buried a few cm deep. Hundreds of samples of 1–10 g and many of 100–1000 g have been recovered. A few samples >1 kg and samples of 20, 23, and 60 kg were recovered according to information received from local residents. Large samples were recovered from 30 to 50 cm below the surface. During a 3-day field reconnaissance from February 8–10, 2013, H. Chennaoui Aoudjehane, M. Aoudjehane, and M. Aboulahris collected approximately 200 g of iron meteorite specimens (Aoudjehane, Aboulahris, personal communication, 2013, areas [1] and [2] in Figs. 2, 3a, and 3b; Table 2). A Russian expedition of six investigators (6–13 March 2013) collected approximately 8.5 kg in total of shrapnel-like and individual samples (areas [1] and [3] in Figs. 2 and 3a; Table 2). In the summer of 2013, about 20 kg of small individual samples and a single mass of approximately 150 kg collected by local residents were presented at the mineral show in Sainte-Marie-aux-Mines, France. A five-person Russian expedition (17–23 March 2014) searched in and around the Agoudal meteorite strewn field and found only two small pieces on the south side of the main valley (area [1], Figs. 2 and 3a), and a 52 kg individual sample in the next valley to the north (area [3], Fig. 3a; Table 2). Numerous fresh pits throughout the area indicate that the strewn field was intensively searched by local residents after March 2013. In discussions with local residents, we were informed that a sample of approximately 100 kg was recovered from a depth of about 2.5 m in 2014.

The total mass of documented finds is 61.98 kg, and the total mass of undocumented finds appears not to exceed 400 kg taking into account the uncertainty of mass estimates. Based on this information, the total recovered mass of the Agoudal iron meteorite can be estimated as no more than 500 kg. It is also possible that additional masses of the Agoudal iron meteorite were collected by local people over time.

Distribution of the Agoudal Meteorite Finds

The locations of finds of documented Agoudal meteorite fragments are reported in Table 2 and shown in Figs. 2 and 3. Numerous small individual samples of Agoudal have been found on the flattened top of the mountain in the east of the scattering area. Point 1 (Table 2) marks the approximate center of a cluster of meteorite finds approximately 600 m in diameter (Fig. 2 and 3a). Samples scattered over an area of about 1 km^2 are buried at 5–15 cm under the surface in loamy sand sediments and have masses from a few grams to a few tens of grams. Around point 1, numerous pits were also found which could be the locations of samples or anthropogenic metal finds recovered by previous searchers. The individual samples which are the result of airborne breakup we recovered around point 1 have classic smooth shapes with regmaglypts (Fig. 4a). Other samples found around point 1 lack defining features of the individual samples and may be described as shrapnel fragments (Fig. 4b). The samples are covered by a brownish layer of terrestrial weathering material approximately 0.05–0.2 mm thick.

Most of the Agoudal finds were located westward of point 1. Two small samples were found at point 2 and a completely rusted sample was recovered from a depth of approximately 20 cm at point 3 (Table 2).

Table 2. Locations of Agoudal meteorite finds and impact structure sites.

Point	N	W	Sample mass(-es)/ total collected mass (g)	Sample shape	Year of find/group	Comments
1	31°59.122′	5°30.005′	/500	I, UN	2013/R	Many small individuals were collected in radius of 300 m; numerous old pits were observed
2	31°59.481′	5°30.515′	8.7, 12.1	UN	2013/M	Samples of 8.7 and 12.1 g were found
3	31°59.525′	5°30.582′	1000	UN	2013/R	Approximately 1 kg rusty sample
4	31°59.247′	5°30.688′	/100	S	2013/R	There are also many old small pits
5	31°59.137′	5°30.707′				Group of old 0.3 m deep pits in a dry channel
6	31°59.232′	5°30.765′	/50	S	2013/R	Many old small pits in a radius approximately 50 m
7	31°59.212′	5°30.955′	—		2013/R	Main outcrop of autochthonous (brecciated limestones with shatter cones) and allochthonous breccias
8	31°59.21′	5°30.943′	—		2013/R	Southern edge of the main outcrop of autochthonous (brecciated limestones with shatter cones) and allochthonous breccias
9	31°59.192′	5°30.927′	—		2013/R	Meter-sized boulders of brecciated rocks
10	31°59.143′	5°30.955′	U	S	2013/M	Some small fragments were collected
11	31°59.096′	5°30.881′	4.6, 1.4	UN	2013/M	
12	31°59.074′	5°30.917′	135	UN	2013/M	60 kg undocumented sample was recovered before by local residents
13	31°59.163′	5°31.006′				Group of old approximately 0.3 cm deep pits in a dry channel
14	31°59.164′	5°31.170′	6.6	UN	2013/M	
15	31°59.097′	5°31.261′			2011?/L	Place (pit) of old undocumented find of 23 kg sample
16	31°59.053′	5°31.201′	500		2013/R	
17	31°59.077′	5°31.48′	1000	UN	2013/R	Approximately 1 kg rusted sample and several small samples found in the old pit
18	31°59.079′	5°31.473′	38	S	2013/M	Possible location of a approximately 10 kg sample
19	31°58.914′	5°31.462′				An empty old pit
20	31°59.69′	5°31.66′	3970	I	2013/R	Northern valley; the sample was recovered from a depth approximately 0.4 m
21	31°59.687′	5°31.658′	2078	I	2013/R	Northern valley; the sample was recovered from a depth approximately 0.4 m
22	31°59.708′	5°31.814′	100	UN	2013/R	Northern valley; the sample was found on the surface
23	31°57.341′	5°29.560′	2.7,1.7, 2.6	UN	2013/M	
24	31°57.390′	5°29.594′	400	UN	2013/M	
25	31°57.433′	5°29.539′	/47	S	2013/M	An undocumented sample <1 kg was found before
26	31°57.412′	5°29.520′	6.8	UN	2013/M	
27	31°57.381′	5°29.534′	3.4, 1.6, 0.3	UN	2013/M	
28	31°57.359′	5°29.525′	3.6, 0.4, 1.3	UN	2013/M	
29	31°57.563′	5°29.141′	6.5, 2.8	UN	2013/M	
30	31°59.694′	5°31.651′	52000	I	2014/R	Northern valley; the sample was recovered from a depth 1.7 m
31	31°59.123′	5°31.097′	7.5	UN	2014/R	
32	31°59.226′	5°29.943′	5.1	UN	2014/R	
CA1	31°59.214′	5°31.054′			2013/M	Outcrop of brecciated limestones with shatter cones
CA2	31°59.300′	5°30.914′			2013/M	Outcrop of brecciated limestones with shatter cones

I = individual fragment; S = shrapnel; UC = unclassified; U = undocumented; M = Moroccan, R = Russian; L = local residents.

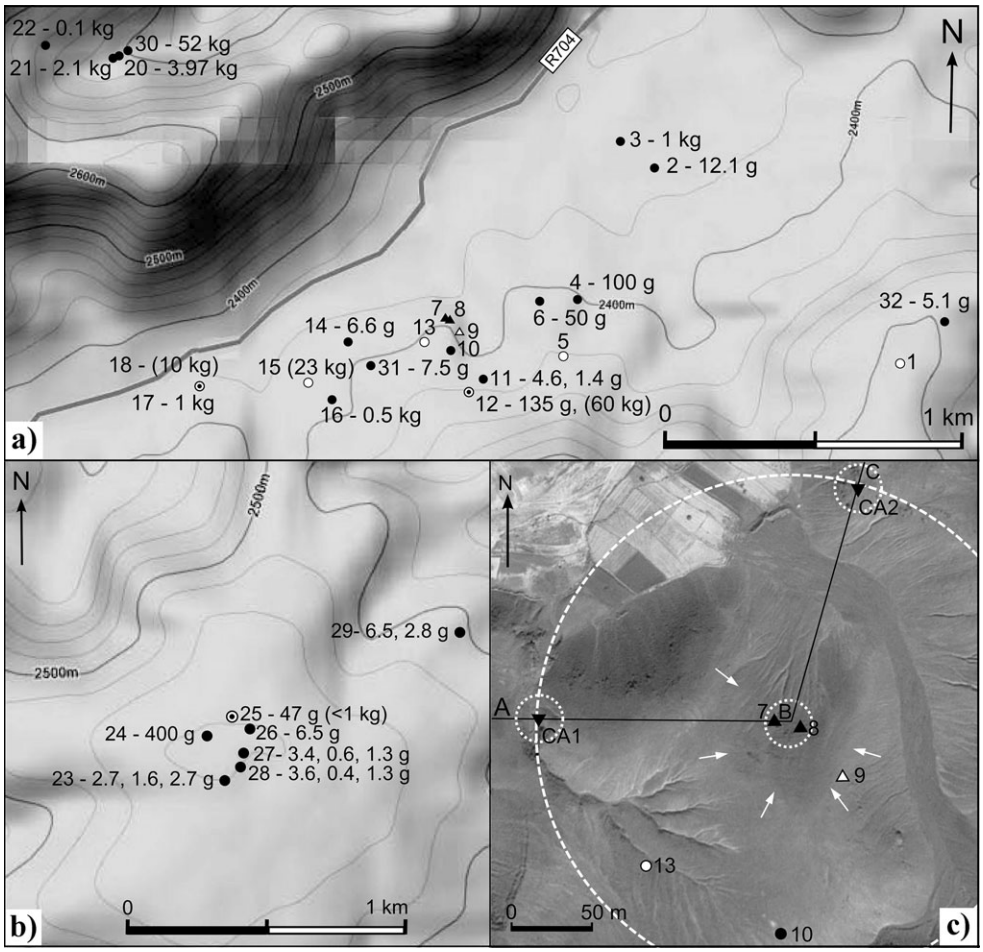

Fig. 3. a) Enlarged section of Fig. 2 showing the distribution of meteorite fragments in the main valley and the northern valley; black circles—finds, white circles—old empty pits, places of possible meteorite finds; white circles with central dot—old pits where the meteorite fragments were found by our teams; black triangles—outcrops of autochthonous and allochthonous breccias with shatter cones; white triangles—outcrops of breccia where shatter cones were not observed. Numerical indexes—location number, mass of find, in parentheses—mass of recent undocumented find. b) Enlarged section of Fig. 2 showing the distribution of meteorite fragments in the southern cluster of finds; the symbols are similar to those at Fig. 3a. c) Satellite image covering the area of the impactite outcrops and nearest finds (image source: Google); inverted black triangles marked as CA1 and CA2—outcrops of autochthonous breccia with shatter cones found by Chennaoui Aoudjehane et al. (2014); dotted circles—approximated contours of the model craters in the crater field scenario (not in the scale); dashed circle—approximated minimal crater of single large crater scenario; white arrows indicate the group of dry channels that could mark a relic of the crater depression; black line marked A-B-C—a line of the cross section (see Fig. 11). Other symbols are the same as those in Fig. 3a and 3b.

Small shrapnel-like and individual-like samples were found on the flattened benches between the wadis, where numerous pits appear to mark previous finds of meteorite samples (points 4, 6). Several pits of approximately 30–50 cm depth, probably excavated by previous collectors to dig out buried specimens, occur in a dry wadi channel (point 5). Point 12 marks the probable find of a 60 kg sample, and 135 g of meteorites were also found at this location. Clusters of old pits were found in the wadi (point 13) and on the flat watershed surface, where several meteorites of total mass approximately 6.6 g were recovered (point 14). The location of a previous find of 23 kg is situated at point 15 (personal communication from local residents, 2011) on the flat wide western side of a wadi. We found a pit approximately 50 cm wide and approximately 30 cm deep there. Small old pits occur frequently around this location. A 500 g sample was found 100 m south of this place (point 16). Point 17 is a pit where a meteorite fragment appears to have been recovered. From this pit, we dug up a further 1 kg meteorite fragment and numerous small pieces of meteorite shrapnel and rust. A possible find location of an approximately 10 kg fragment occurred near this pit

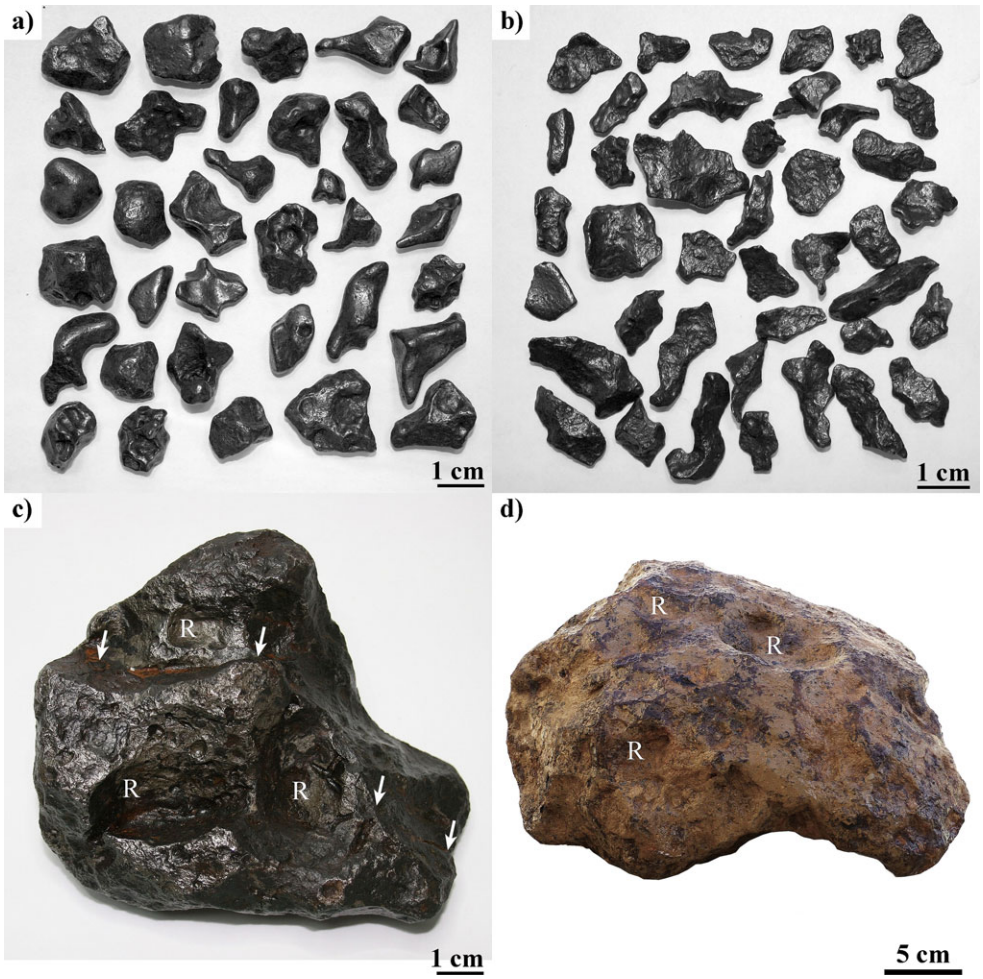

Fig. 4. Morphology of the Agoudal meteorite fragments: a) individual meteorite samples, mostly collected around the point 1; b) shrapnel fragments; c) the 2.1 kg sample found in the northern valley (point 21); white arrows mark a crack running through the whole sample that could be a result of atmospheric or impact deformation; R—the elliptical cavities on the surface of the sample, which could be the regmaglypts; d) the 52 kg sample found in the northern valley (point 30); the symbols are the same as those in Fig. 4c.

(point 18), and a sample of 38 g also was found there. An old pit at point 19 was found empty.

Large finds recovered from the soil are heavily oxidized and in some cases we cannot distinguish individual airborne samples from shrapnel. Four meteorite fragments were recovered approximately 1.5 km to the northwest of the approximate center of the main cluster of finds, in the next valley (the "northern valley"). The northern valley is V-shaped in cross section and is generally dry, with intermittent streams. Fragments of 3.97 and 52 kg (points 20, 30) were excavated from a depth of approximately 0.7 and 1.5 m, respectively; they were found between meter-sized alluvial boulders in the valley bed. Smaller meteorite finds (2.1 kg, point 21; 0.1 kg, point 22) were deposited in the surface layer of alluvium of the same valley. These meteorites could have been transported to their present locations from a watershed dividing the main and northern valleys, and/or could have been transported from the western parts of the northern valley. The northern finds differ in shape from the classic individual samples of an iron meteorite shower. They are flattened with rounded edges that do not completely match typical shrapnel fragments, which usually are splinter-shaped with sharp ragged edges. The northern samples were found buried in alluvial cobble deposits, so the original fragment shapes may have been altered through mechanical grinding by stones. However, the 2.1 and 52 kg northern finds (Figs. 4c and 4d) is clearly an individual fragment with a minor degree of oxidation and a regmaglypted surface. The northern valley was searched systematically and no traces of previous excavations of meteorites were found. This may suggest an original low density of meteorite

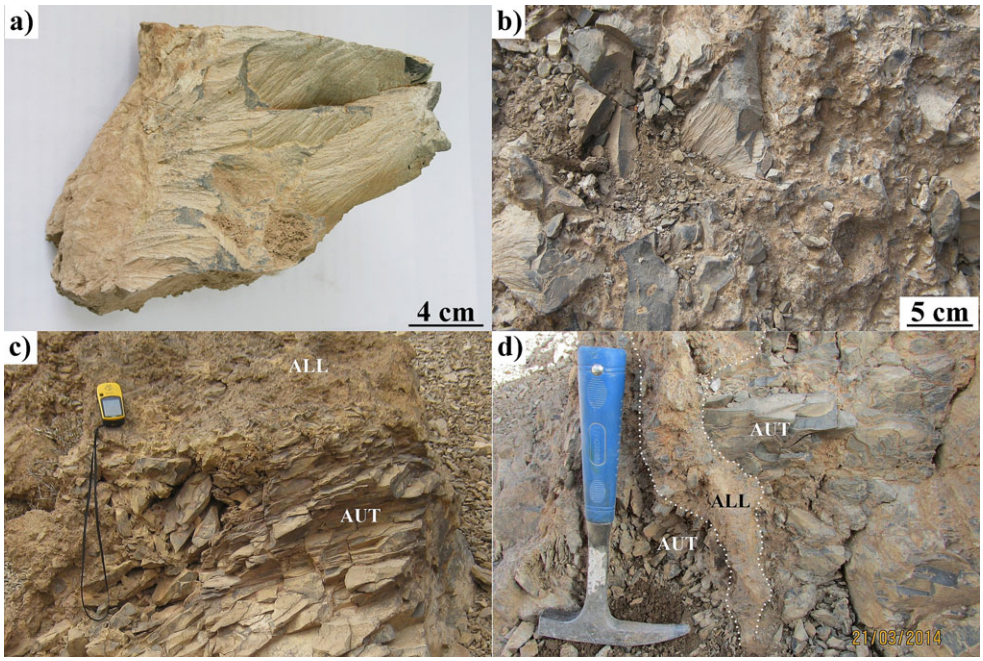

Fig. 5. Shocked target rocks and impactites of the main outcrop (point 7) of the impact structure, found near Agoudal: a) sample of shocked limestone with shatter cones from the autochthonous breccia; b) medium- to coarse-grained allochthonous breccias covering the target rocks; the breccias contains the clasts with shatter cones (near the center of the image); c) contact of auto- (AUT) and allochthonous (ALL) breccias; d) a vein of allochthonous breccia protruding into the autochthonous breccias; the vein is shown by dotted line, the symbols are the same as those in Fig. 5c.

distribution in this part of the Agoudal meteorite scattering area. Another group of meteorite finds (points 23–29, Table 2) was situated approximately 3.3 km south of point 1, outside the main valley on the flat top of a mesa including an old pit where approximately 1 kg sample was recovered by local residents (point 25). These samples cannot be clearly identified as either individual fragments or shrapnel.

Geology of the Impact Structure

The remnants of an impact structure are situated within the strewn field of the Agoudal iron meteorite near the bottom of the main valley (Figs. 2, 3a, and 3c; Table 2). The presence of the impact structure was recognized by the occurrence of numerous limestone fragments with shatter cone texture in a dry wadi. We searched for the source of the shatter cone material and found an outcrop ("main outcrop") of brecciated limestones with shatter cones, and polymict breccias on the left (northwestern) side of the wadi, on the slope of an approximately 20 m high, 20–30 m long, north–south-oriented hill (points 7 and 8, Table 2; Figs. 2, 3a, and 3c). Meter-sized boulders of brecciated rocks were observed up to 70 m to the south of the main outcrop (point 9, Table 2; Fig. 3c), but none were observed on top of the hill or to the north of the main outcrop or on the other neighboring hills. No crater rim was seen in field investigations or on satellite images. The outcrop is located within the mildly sloping watershed collection area of the eastern slope of the hill. The area opens downward onto the hill slope and is surrounded by watersheds from other sides and potentially could represent a relic of the crater (Fig. 3c); or potentially could be a part of highly eroded syncline. Two other outcrops of limestones with shatter cones were found by a Moroccan-European expedition in October 2013 (points CA1, CA2 in Fig. 3c; Table 2; Chennaoui Aoudjehane et al. 2014).

The basement rocks of the Agoudal impact structure are Jurassic sedimentary rocks of the Binelouidane Marly Limestones Formation of Bajocian (Middle Dogger) age, made up of dark gray marl and limestone. In the bottom of the main impactite outcrop, intensively fractured target rock has prominent shatter cones 1–30 cm in size, grouping into at least four differently oriented systems (Fig. 5a).

At the main impactite outcrop (points 7 and 8), fractured and brecciated limestones are covered by medium- to coarse-grained polymict breccia (Fig. 5b) of up to 0.5 m thick. The visible contact of the breccia layer with the bedrock is sharp and relatively straight

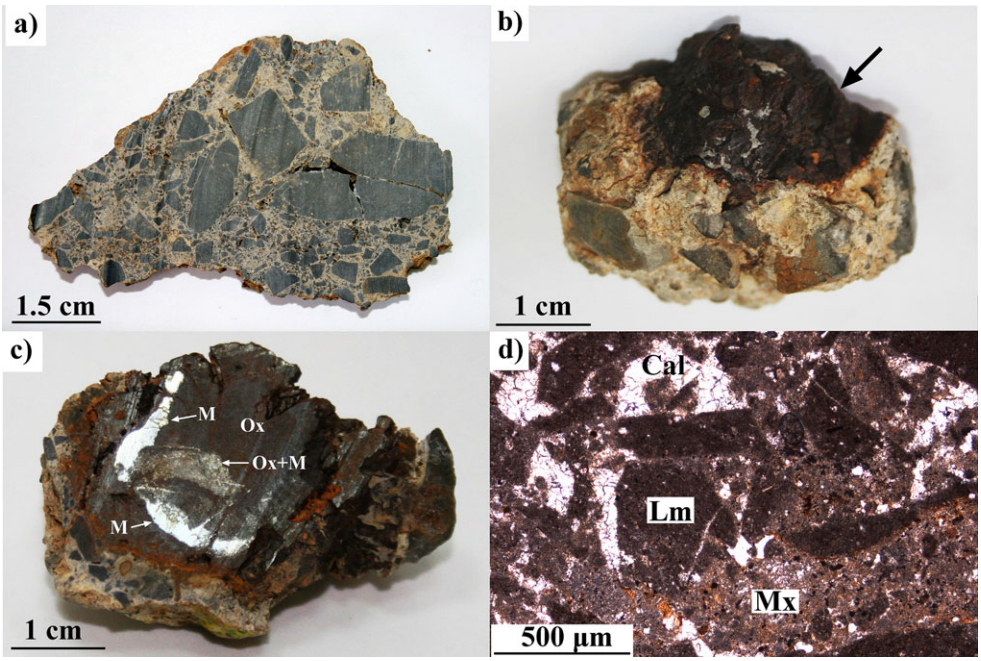

Fig. 6. a) Cut sample of autochthonous breccia from the Agoudal impact structure; b) fragment of the breccia with inclusion of oxidized meteorite iron (shown by arrow); c) cut sample of the Agoudal breccia with the inclusion of oxidized iron. Ox = Fe-Ni hydroxides; M = Fe-Ni metal; Ox+M = incompletely weathered area of the metal composed by metal-oxide aggregate; d) optical image of structure of the polymict breccia. Interstitial spaces between the limestone fragments (Lm) are partly filled with fine-grained clastic carbonate material (Mx), partly empty, and mostly filled by aggregate of subhedral transparent calcite crystals (Cal); transmitted light, crossed polars. All images are from the main crater outcrop (point 7).

(Fig. 5c); at places, the polymict breccia forms veins 1–2 cm thick and approximately 30 cm of visible length vertically protruding through the fractured bedrock (Fig. 5d). Shatter cones occur widely within the marl and limestone fragments of the polymict breccia from the main outcrop, but were not found in the breccia boulders occurring approximately 70 m south (point 9). The hill slope below the impactite outcrop is covered by sand-clay and gravel sediments, which are partly degraded by a set of dry drains approximately 30 cm deep. We found fragments of polymict breccias, removed downslope from the main outcrop, at approximately 20–30 cm depth in the layer of unconsolidated sediments covering the middle and lower slope.

Beside the polimict breccia of the main outcrop, we found other types of brecciated rocks out to as much as approximately 2 km from this main outcrop, for example, we observed a thin (approximately 10–20 cm) layer of calcrete-like, well-sorted, medium-grained breccias about 100–150 m west of the main outcrop. These breccias were different in texture and composition from the polymict breccia, and appear to probably be the product of weathering of unshocked limestone, downslope transport, resedimentation and lithification of the limestone fragments by evaporitic minerals in the arid surface environment.

Petrography and Mineralogy of the Polymict Breccia

Macroscopically, the fine- to medium-grained polymict breccia (Fig. 6a) in contact with brecciated limestones bearing shatter cones is composed of dark gray, sharply angular elongated and isometric limestone fragments up to approximately 10 cm in size, combined with more fine-grained, light gray material with abundant empty pores. The grain size distribution of the breccia, determined by macro- and microscopic investigations, is reported in Table 3. Some breccia boulders in the same outcrop are enriched in coarse fragments (>10 cm) in a matrix of less coarse-grained breccia. We cannot report the relative distribution and relationships of different breccia types because the outcrop is partly covered by unconsolidated sediments. Rare samples of the breccia from the main outcrop contain partly oxidized fragments of meteorite iron approximately 1–3 cm in size (Figs. 6b and 6c).

The fragments in the polymict breccia are sharply angular and not sorted by size. No breccia-in-breccia fragments were observed. The breccia consists of two dominant kinds of carbonate rocks (1) fine-grained, poorly transparent carbonate rock; and (2) coarser grained carbonate rock, more transparent, and rarely consisting of detrital debris. Interstitial spaces between rock fragments are partly filled by fine-grained, probably

Table 3. Grain size distribution of polymict breccias from the main impactite outcrop.

Grain size (cm)	vol%
2–4	17.7
1–2	13.7
0.5–1	17.0
0.2–0.5	7.2
0.1–0.2	6.9
0.05–0.1	8.6
0.02–0.05	8.2
0.01–0.02	2.2
<0.01	18.6
Total	100.0

clastic carbonate material, partly empty, and filled by an aggregate of subhedral transparent calcite crystals (Fig. 6d). The calcite appears to have crystallized from carbonate-rich water infiltrating through the breccia, cementing it. Some large limestone fragments are crossed by rare narrow calcite-filled veinlets. The accessory phases of the breccia are tiny grains of quartz, feldspar, Fe-sulfide, chromite, and glauconite. Inclusions of biogenic iron oxide observed in the limestone fragments and in the breccia matrix are represented by framboidal clusters of 5–20 μm spherical grains or zonal euhedral crystals. Rare, more coarse-grained aggregates of Ni-free iron hydroxides without any ordered texture were found in the matrix of the breccia. Quartz grains observed in thin sections and in HCl dissolution residue of the breccia and target limestones are mostly free of planar deformation features (PDF). Only two approximately 25 μm quartz grains with one definite set of subparallel thin lamellar features with step 0.5–1 μm was found in thin sections of the polymict breccia. The thickness of the lamellae is <1 μm. It is unclear whether these lamellae are PDF or not.

Minor components of the breccia are polymineral inclusions of amorphous and cryptocrystalline phases, colored light brown in transmitted light. The inclusions occur in interstitial spaces of lithic clasts as rare objects of irregular, isometric, or vermicular shape (Fig. 7a), at places joining together the large lithic clasts as contact cement, or as thin discontinuous layers covering the limestone fragments (Fig. 7b), without evidence of textural or chemical changing of the limestone at the contact. The size of the inclusions is in the range of 50–1000 μm. Large inclusions usually contain rock fragments (limestones) and mineral grains, mostly quartz, feldspar, and iron oxides; some of them contain small vesicles (Fig. 7c).

Several similar inclusions were analyzed in the thin sections of the breccia sample from the main impactite outcrop (point 7) for rock-forming and minor element abundances (Table 4) (1) inclusion #1–1 is a 900 μm wave-shaped object located along the margin of a limestone fragment; it is fluidal-textured and contains rare grains of quartz and feldspar (Figs. 7a and 7d); (2) inclusion #1–2 is 600 μm in size and is full of small grains of quartz, feldspar, and limestone (Fig. 7a); (3) inclusion #2 is 250 μm in size; it occurs on the contact of two limestone fragments; the interstitial space of the breccia around the inclusion is empty; the inclusion is red-brown in transmitted light, free of mineral inclusions and has massive texture (Fig. 7b); (4) inclusion #3 is 300 μm in size, comprised of an aggregate of cryptocrystalline phases with tiny mineral inclusions (Figs. 7e and 7f).

All of the analyzed inclusions have low analytical totals that are not correlated with CaO (as a component of carbonate with undetermined CO_2), suggesting that the objects contain significant amounts of water. Most of the inclusions are enriched in Si and Al and depleted in Ca, in contrast to the target carbonate rocks, but some Ca-rich and intermediate compositions also are present (Table 4). Concentrations of CaO that should reflect the carbonate component of the inclusions are varied. A compositional profile performed through inclusion #3 across its border with fine-grained carbonaceous-rich matrix indicates correlated variations of CaO and other rock-forming elements in the melt. The carbonate breccia matrix contacting with inclusion #3 contains small inclusions (#4–1, 2, 3, Table 4) with compositions close to that of the larger inclusions.

CaO content of the inclusions has direct negative correlations with SiO_2 content (Fig. 8a) and Al_2O_3 content (Fig. 8b). All other rock-forming oxide contents are positively correlated among themselves, SiO_2 and Al_2O_3, with the exception of Na_2O (Fig. 8c). SiO_2/Al_2O_3 ratios of low-Ca inclusions are similar to that of high-Ca ones and target limestone (Table 4). However, the SiO_2/FeO ratio of Si-Al-rich inclusions is two-fold lower than that of Ca-rich ones and target rocks (Table 4). The Si-Al-rich inclusions are depleted in Na, and enriched in K, which has a positive correlation with Al (Fig. 8d). The bulk compositions of the inclusions are not stoichiometric and most resemble heterogeneous mixtures of carbonate and silicate materials.

Chemical Composition of the Agoudal Iron Meteorite and the Iron Enclosed in the Impact Breccia

The results of investigation of two Fe-Ni metal areas on the iron from the breccia and one Fe-Ni metal area of the Agoudal meteorite from the strewn field showed that they are similar (Table 5), have the same geochemical patterns, and are nearly identical to results obtained by Chennaoui Aoudjehane et al. (2013). Plots of Au versus Co, Ni, Ga, Ge, As, and Ir (Fig. 9) show that the Agoudal iron meteorite and the breccia iron

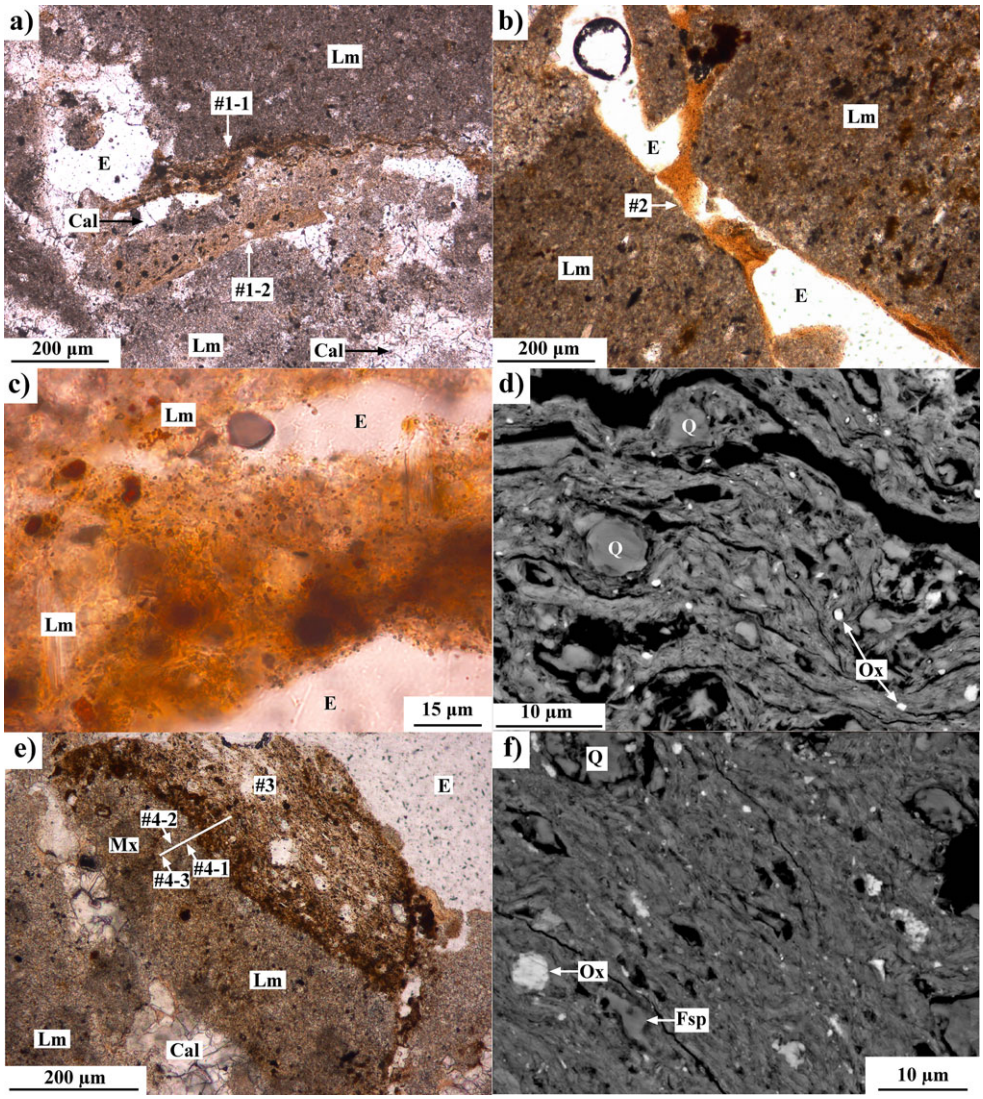

Fig. 7. Microscopic views of micro- and cryptocrystalline inclusions in the allochthonous breccia, possibly relics of weathered impact melts (see also Table 4): a) fluidal-textured and massive-textured clast-loaded inclusions (#1–1 and #1–2 respectively); b) massive-textured inclusion #2 and the similar material, covering the limestone fragments as a thin discontinuous layers; c) vesicles in the cryptocrystalline inclusion (in the central part of the image) from the allochthonous breccia; transmitted light optical images; d) backscattered electron image of a fluidal-textured inclusion #1–1 containing tiny mineral inclusions; e) microscopic view of inclusion #3 (transmitted light), white line is analytical profile across a contact of the inclusion #3 and clastic breccias matrix; locations of inclusions 4-1, -2, -3 on the profile are shown by an arrows; f) backscattered electron image of the inclusion #3. Ox—Ni-free iron hydroxide, Fsp—feldspar, Q = quartz, E = empty interstitial spaces of the breccia, other symbols are the same as those in Fig. 6.

plot together with other members of the IIAB irons (Wasson et al. 2007).

Estimate of Impact Velocity and Mass of the Crater-Forming Impactor

The planar impact approximation (Melosh 1989, p. 54) allows estimation of maximum shock pressure after an impact with a given velocity and a certain combination of projectile/target materials. Using Hugoniot data for calcite and iron (Trunin et al. 2001), we calculated shock pressures for various impact velocities (Fig. 10a; Table 6) and then, using an atmospheric entry model without fragmentation, we estimated the meteoroid mass which allows impact with a given velocity (Table 6). The presence of shatter cones as well as the absence of PDF, indicating pressure range 2–5 GPa (Stöffler and Langenhorst 1994; French 1998), requires impact velocities lower than 0.6 km s^{-1} and higher than 0.27 km s^{-1}. The lowest velocity of 0.27 km s^{-1}

Table 4. Compositions of different materials from the Agoudal breccias, obtained by the electron microprobe.

	SiO_2	TiO_2	Al_2O_3	Cr_2O_3	FeO	MnO	MgO	NiO	CoO	CaO	Na_2O	K_2O	Total	SiO_2/CaO	SiO_2/Al_2O_3	SiO_2/FeO
1	2.56	0.00	0.78	<0.02	71.7	0.06	0.98	0.13	0.16	0.65	<0.02	<0.02	77.0			
2	40.6	1.63	18.2	0.03	7.19	0.04	4.97	0.02	<0.02	0.80	0.52	4.07	78.1	51	2.2	5.6
3	30.5	0.99	11.9	0.03	5.26	0.05	3.85	<0.02	<0.02	15.8	0.08	2.86	71.3	1.9	2.6	5.8
4	11.7	0.27	4.69	<0.02	3.17	0.03	1.36	<0.02	<0.02	25.6	0.10	0.73	47.6	0.5	2.5	3.7
5	42.0	0.47	22.8	0.04	6.31	0.02	3.75	<0.02	<0.02	1.24	0.13	4.49	81.3	34	1.8	6.6
6	39.8	0.86	24.9	0.04	8.85	<0.02	7.12	0.05	0.03	0.53	0.18	5.06	87.5	75	1.6	4.5
7	41.1	0.31	17.6	0.03	7.06	<0.02	4.70	<0.02	0.02	1.73	0.23	4.01	76.8	1.1	2.3	5.8
8	17.6	<0.02	13.5	<0.02	11.9	<0.02	3.27	0.02	0.02	25.1	0.17	1.88	73.4	0.7	1.30	1.5
9	38.3	0.43	20.6	0.04	8.54	0.03	5.45	<0.02	0.02	7.34	0.11	4.62	85.4	5.2	1.9	4.5
10	24.4	0.55	17.0	0.02	5.24	<0.02	3.94	0.02	<0.02	21.2	0.13	3.59	76.2	1.1	1.43	4.6
11	5.73	0.18	2.63	b.d.	2.70	0.02	1.10	<0.02	<0.02	44.3	0.15	0.41	57.2	0.1	2.2	2.1

1: Fe hydroxides in matrix; 2: Inclusion #1–1 (fluidal-textured): Ca-poor areas (average of 6 defocused analyses); 3: Inclusion #1–1: Ca-rich area defocused; 4: Inclusion #1–2 (massive, clast-loaded) (average of five defocused analyses); 5: Inclusion #2 (homogeneous) (average of three defocused analyses); 6: Inclusion #3 (massive, clast-loaded) defocused; 7: Inclusion #3 profile, average of six focused analyses; 8, 9, 10: Inclusions #4–1, 2, 3 occurred in the carbonate-rich matrix contacting with inclusion #3 (focused analyses); 11: Limestone (average of two defocused and four focused analyses).

Table 5. Chemical composition of the Fe-Ni inclusion in the polymict breccia and a sample of Agoudal meteorite, measured by LA-ICP-MS (μg g^{-1}).

Sample	Description	P	S	Cr	Fe	Co	Ni	Cu	Ga	Ge	As	Mo
A2	Meteorite	3245	41	10	939154	4845	52232	98	52	137	7.42	7.97
A3 + 4	Fe-Ni inclusion	3033	88	5	939131	4774	52543	94	49	124	7.95	7.71
A5	Fe-Ni inclusion	4078	279	5	939408	4758	50729	94	51	129	8.23	8.71
Agoudal (Chennaoui Aoudjehane et al. 2013)	Meteorite					4100	55000		58			

		Ru	Rh	Pd	Sn	Sb	W	Re	Os	Ir	Pt	Au
A2	Meteorite	4.77	1.74	2.25	0.226	0.088	0.755	0.0024	0.0150	0.0194	5.53	0.943
A3 + 4	Fe-Ni inclusion	3.63	1.61	2.30	0.227	0.089	0.573	0.0023	0.0143	0.0189	3.91	0.993
A5	Fe-Ni inclusion	3.72	1.65	2.33	0.428	0.094	0.623	0.0022	0.0157	0.0190	4.03	1.00
Agoudal (Chennaoui Aoudjehane et al. 2013)	Meteorite									<0.04		1

corresponds to an impactor mass of approximately 50 kg. Assuming that the planar features found in two quartz grains are true single systems of PDF, the maximum estimated shock pressure should be higher, at least 5–10 GPa (Stöffler and Langenhorst 1994; French 1998), requiring an impact velocity of 1 km s^{-1} and an impactor weighing approximately 150 kg. Shock pressure of approximately 30 GPa (onset of melting along fissures) demands an impact velocity of 2.5 km s^{-1} and, hence, a main fragment with mass of approximately 500–1000 kg (Table 6). The total mass of all fragments could be substantially higher than the amount of material recovered so far, if intense fragmentation took place during the atmospheric entry.

Strewn Field Model

Distribution of meteorites and impact craters on the surface depends on the entry angle, preatmospheric mass of an iron meteoroid, and its strength. We vary preatmospheric meteoroid diameters from 1.4 to 8 m. Strength of a meteoroid above the atmosphere as well as strength of all fragments are defined by Weibull statistics (strength decreases with mass increase); we also allow moderate deviations of individual fragments' strength from pure exponential dependence (Artemieva and Shuvalov 2001). Thus, similar initial conditions (such as size and impact angle) may result in different final results, which we designate in this section as low-, medium-, and high-strength projectiles. Numerous small fragments (<0.1 kg) are excluded from the model to simplify the output. Crater diameters are estimated according to scaling laws (Holsapple and Housen 2007).

Figure 10b shows a few possible scenarios calculated for two relatively small, 1.4–1.8 m, preatmospheric diameters of the Agoudal meteoroid and entry angles of 60° and 45°, respectively.

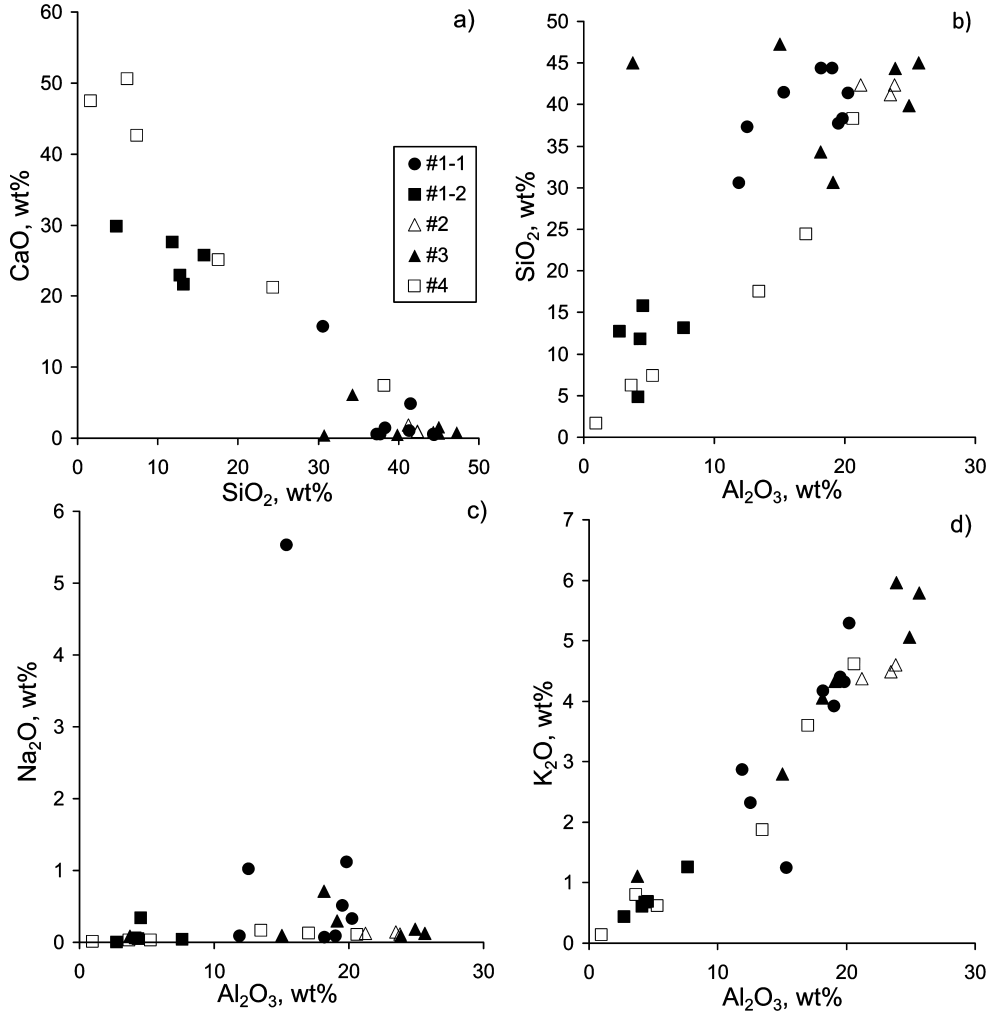

Fig. 8. Rock-forming components in the inclusions that could be the relics of weathered impact melt in the breccias: #1–1—fluidal-textured inclusion; #2—homogeneous massive-textured inclusion; #1–2 and #3—massive, clast-loaded inclusion; #4—small inclusions in the carbonate-rich matrix contacting with inclusion #3. The symbols for Fig. 8b–d are the same as those in Fig. 8a.

Computer simulations of strewn field formation show that the scattering area length could range from 5 km (the entry angle of 60°, A1-C1 in Fig. 10b) to 11 km (the entry angle of 45°, A–C in Fig. 10b). The number of individual fragments strongly increases with decreasing meteoroid strength. In scenario A1, the meteoroid strength is low, resulting in a large amount of relatively small (<80 kg) and slow (<1 km s^{-1}) fragments. On the contrary, in scenario C1, the strength is high; a few high-velocity fragments reach the surface creating a crater field without meteorites. In scenario B1 (1.4 m diameter body, entry angle 60° to horizon, medium strength), the total final mass of the meteorite fragments slightly exceeds 550 kg; the largest, crater-forming fragment weighs 460 kg and reaches the surface with a velocity of 3.2 km s^{-1}; another four have masses >10 kg and impact velocities of 0.1–0.2 km s^{-1}. At a more shallow entry angle of 45° (frames A–C in Fig. 10b), strewn fields are much longer, up to 11 km, except for the strongest meteoroid in scenario C, in which, similar to C1, craters, but not meteorites, may be found on the ground. The estimated parameters and number of large finds in scenario B1 are in good agreement with observed parameters of a small (only one impact crater) Agoudal strewn field.

Figure 10c depicts strewn fields created by a larger, 2–4 m in diameter, projectile entering the atmosphere at 45°. The largest fragments are always in the downrange part of the strewn field; the length of all strewn fields is approximately 7 km (would be longer if smaller, <0.1 kg, fragments included in the model). Figure 10d

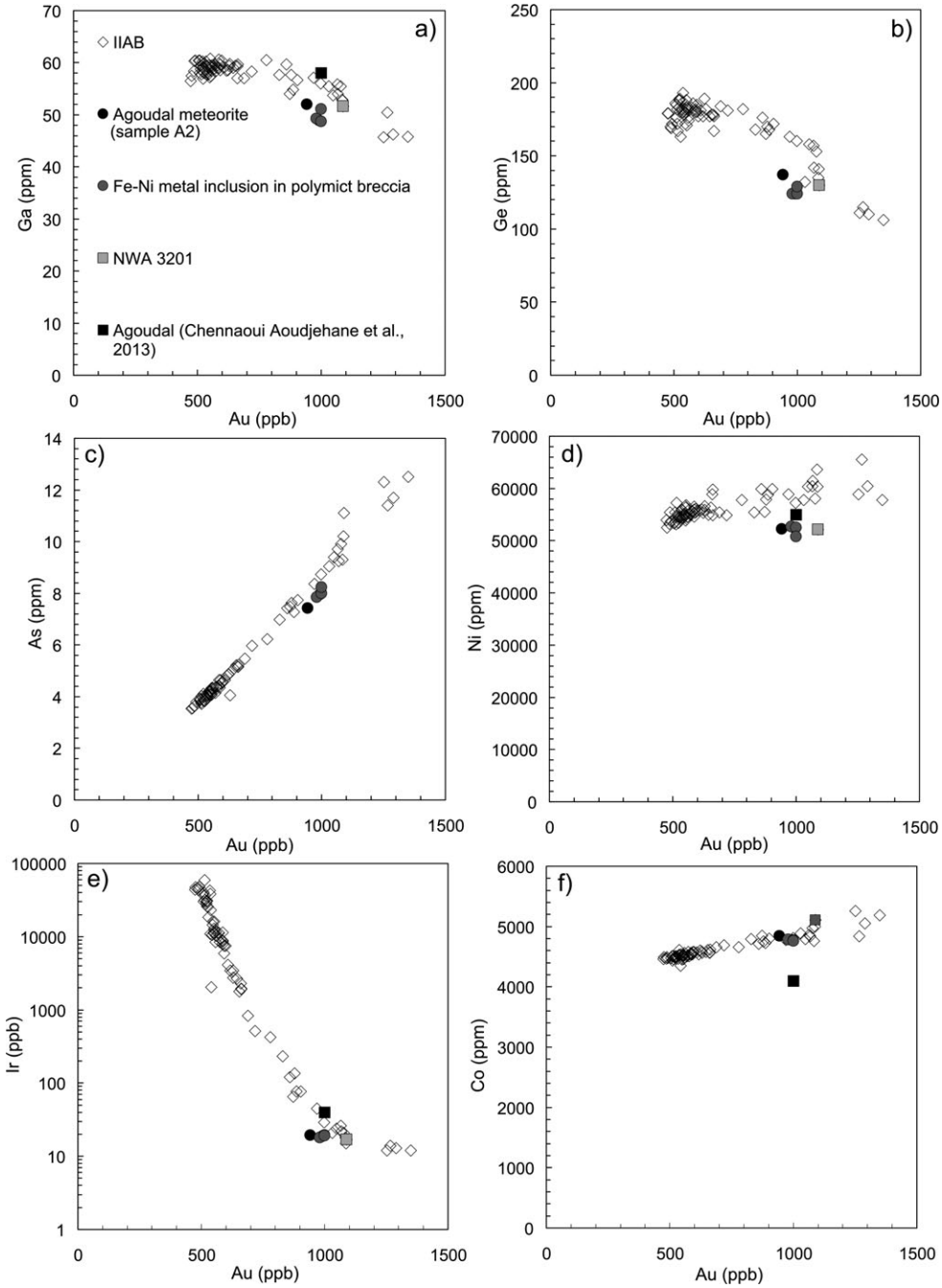

Fig. 9. Concentration of Au versus trace elements and Ni abundances of Agoudal iron meteorite and iron fragment embedded into allochthonous breccia. Data were obtained using LA-ICP-MS. Data for IIAB NWA 3201 (Wasson et al. 2007) are shown for comparison (see the text). The symbols for Fig. 9b–f are the same as those in Fig. 9a.

illustrates the central part of crater fields for projectiles 2–8 m in diameter entering the atmosphere at 45°. All crater fields are similar in size (approximately 500 m); medium-sized projectiles (2–4 m) produce strewn fields of closely packed craters; the largest projectiles (6–8 m in diameter) produce clusters which resemble a single shallow crater (Fig. 10d). Calculated impact velocities of the largest fragments in this scenario are between 1 and 6 km s^{-1}, allowing formation of shatter cones, PDF, and partial melting.

Table 6. Estimated impact velocity, transient crater diameter, and maximum shock compression in the target as a function of the preatmospheric fragment size.[a] Preatmospheric velocity is 18 km s^{-1}, entry angle—45°, projectile type—iron.

Initial diameter (m)	Initial mass (kg)	Final/initial mass ratio	Impact velocity (km s^{-1})	Crater diameter (m)[b]	Expected maximum shock pressure (GPa)[c]
10	4.1×10^6	0.8	15.5	330	293
8	2.1×10^6	0.76	14.8	260	270
6	8.8×10^5	0.69	13.9	190	243
4	2.6×10^5	0.54	11.9	112	187
3	1.1×10^5	0.42	10.0	99	141
2.7	8.0×10^4	0.37	9.2	60	123
2.5	6.4×10^4	0.33	8.5	51	108
2	3.1×10^4	0.21	6.4	31	69
1.8	2.4×10^4	0.14	5.3	22	53
1.6	1.7×10^4	0.07	3.9	13.6	34
1.4	1.1×10^4	0.04	2.3	7	17
1.2	7.1×10^3	0.02	0.93	3	5.50
1	4.1×10^3	0.011	0.21	1	1.1
0.8	2.1×10^3	0.004	0.11	0.4	0.6

[a]We assume that the largest fragment survives the entry without further fragmentation. Thus, its diameter is not equal to a diameter of the whole body, which depends on a degree of fragmentation; however, it may be considered as the lowest limit of the total preatmospheric size.
[b]Based on scaling laws (Holsapple and Housen 2007) for strength-dominated craters in competent rocks.
[c]The planar impact approximation is used to calculate this value. Only a vertical component of the impact velocity is taken into account. An impact angle is equal to the entry angle (i.e., the trajectory is a straight line) for all sizes except of the smallest two, in which impact angles are 55° and 87°, respectively.

Impact Crater and Ejecta Distribution

Because the impactite outcrop was found on the slope of a hill, the preimpact inclination of the target should be emphasized as an important parameter for numerical modeling of impact crater formation, especially for the impact ejecta distribution. Using the SOVA program code for a simulation of minimal possible crater formation resulting in the observed shock effects, we modeled the initial stage of a 2.5 km s^{-1} impact of a 60 cm diameter iron sphere (mass of 870 kg) at 45° to the horizon into a 30° slope (i.e., a 75° impact relative to the slope). The target consists of sedimentary rocks described by the equation of state for calcite. Our results show that at these entry parameters at least 1 m^3 of target rocks (10 times the projectile volume) could be compressed between 2 and 6 GPa, i.e., these rocks represent potential shatter cones. The amount of melt (peak shock pressure >30 GPa) at these conditions should be small, <0.02 m^3. The estimated transient cavity size in this case could be estimated as approximately 15 m, with a final crater diameter of approximately 19 m. However, if the impact occurs in sloping target terrain, the transient cavity is unstable (Elbeshausen et al. 2013). The slope is likely to collapse and fill the crater with fragmented target material (breccia) which will bury iron fragments at a calculated depth of approximately 5 m (we did not calculate this stage). Due to the highly eroded state of the impactite outcrops and uncertainties of the entry data, the calculated parameters of the Agoudal impact structure gave only a minimum estimation of the size of an impactor that would have been capable of forming a relatively small crater and producing the observed shock effects.

The numerical modeling produced estimates of ejecta distribution around the crater, both target rocks and projectile fragments. Tracer particles' velocities and ejection angles are recorded at the moment of ejection. Then, we make a reasonable, albeit simplified, assumption for the size-frequency distribution of ejected fragments: the fragment size is inversely proportional to the value of its maximum shock compression (Shuvalov 2002). Ballistic continuation assuming interaction of fragments with the atmosphere is used to find the fragments' final position. We also take into account the fact that the impact could occur on a slope. Obviously, the distribution of projectile ejecta around a small crater is strongly influenced by the atmosphere. Large, high-velocity ejecta fragments (approximately 4 kg in estimated mass with a velocity of 0.5–1 km s^{-1}) could travel up to 3 km from the crater, while small fragments (a few grams) ejected with similar velocities could be deposited within a 100 m radius area near the crater (Fig. 10e) due to atmospheric friction. In the case of oblique impact into

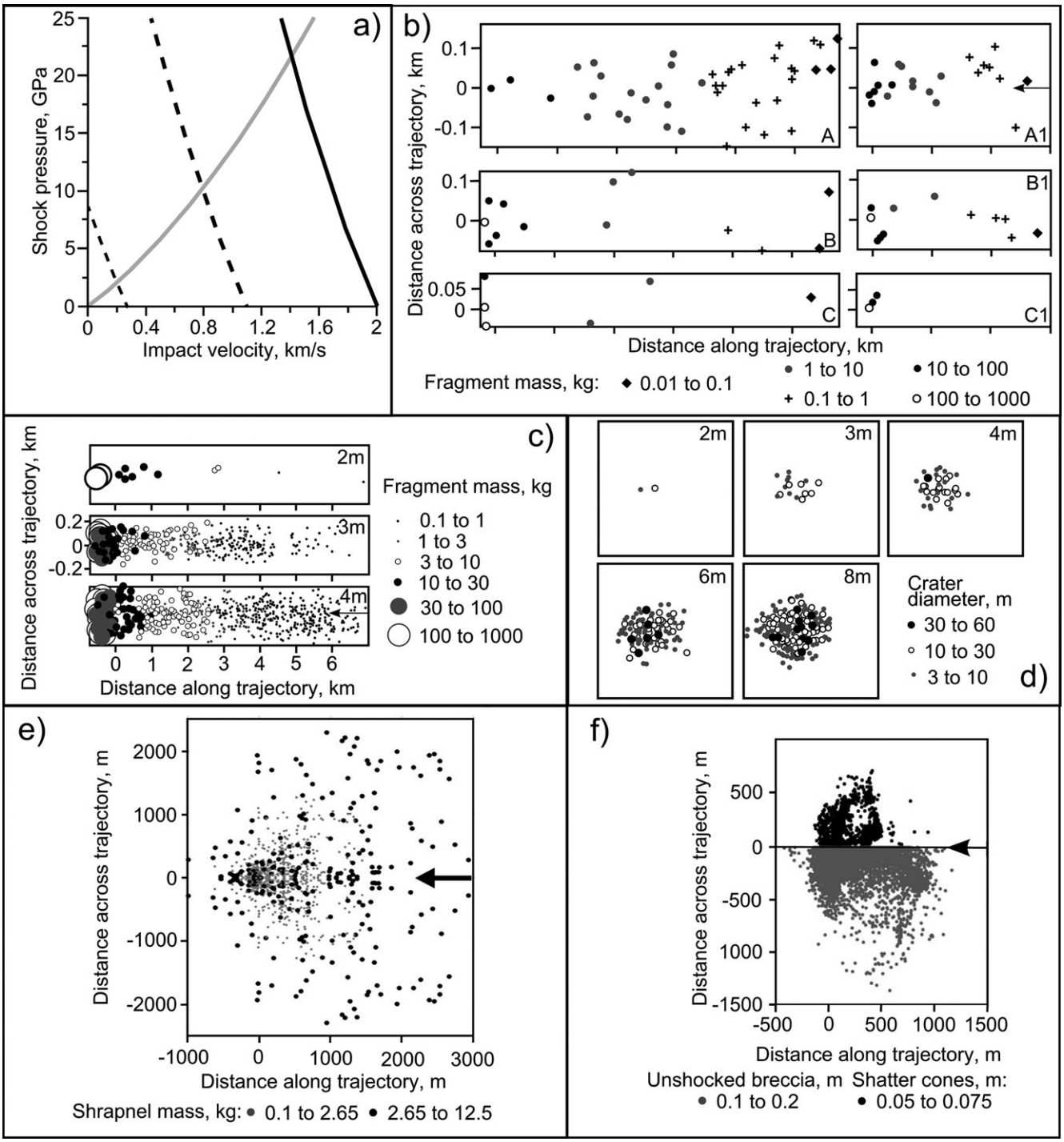

a target inclined toward the meteoroid trajectory, projectile ejecta should be deposited mainly uprange. These ejecta (shrapnel) should overlay the strewn field of the simulated meteoroid. The farthest downrange fragment may be found at a distance of 1 km. Both shocked (with shatter cones) and nonshocked target materials ejected from the crater are concentrated uprange even prior to the crater collapse and possible avalanche on the target slope. As the target density is approximately three times smaller than the projectile density and ejecta are strongly decelerated by the atmosphere, the total area of target ejecta is substantially smaller than the area covered by the projectile ejecta (Figs. 10d and 10e).

Fig. 10. a) Intersection of calcite Hugoniot (thick gray line) with iron Hugoniot curves for impact velocities of 2 km s^{-1} (black solid line), 1.1 km s^{-1} (dashed line), and 0.27 km s^{-1} (dotted line). Corresponding maximum shock pressures are 22, 10, and 2 GPa respectively. b) Proposed models of the Agoudal strewn field. The left column shows strewn fields created after a 1.6 m diameter projectile atmospheric entry at 45° to horizontal; the right column shows strewn fields for a 1.4 m diameter projectile entry at 60° to horizontal. The projectile strength varied randomly (with an average value of $4.4 \cdot 10^7$ Pa for a 1 kg sample). Variants A and A1 correspond to a weak projectile (many small fragments), variants C and C1 correspond to a strong projectile (fewer fragments, high final velocities), and variants B and B1 with an intermediate projectile strength fit observations reasonably. c) Iron meteorites distributions, resulting from fragmentation of 2–4 m in diameter iron projectiles in the atmosphere. Black arrow shows an impact direction. The downrange parts of each strewn field are shown in Fig. 10d (the largest fragments produce not meteorites but craters and shrapnel). All distances are in km; scaling of X (along the trajectory) and Y (across the trajectory) axes are different. d) Crater fields produced by iron projectiles with diameters from 2 to 8 m entering the atmosphere with a velocity of 18 km s^{-1} at an angle of 45°. The size of each plate is 1 × 1 km. e) Calculated projectile ejecta distribution around the crater with coordinates (0,0). The impact direction is shown by a black arrow; f) the distribution of target ejecta around the crater. An upper plate shows a distribution of the target fragments compressed in the range 2–5 GPa (possible shatter cone creation), bottom plate shows target ejecta subjected to lower shock pressure. The crater is at the point (0,0), the impact direction is shown by a black arrow. Impact angles are 45° and 60° for a small impact scenario (Fig. 10b) and 45° for all other scenarios (Fig. 10c–f).

Table 7. Bulk chemical composition of Agoudal target rocks and allochthonous breccia, measured by XRF (wt%) and abundances of Ni and Co in these rocks measured by ICP-MS (μg g^{-1}).

	Na_2O	MgO	Al_2O_3	SiO_2	P_2O_5	K_2O	CaO	TiO_2	FeO	LOI[b]	Ni	Co
Target limestone[a]	0.35	1.10	3.20	9.99	0.05	0.54	46.81	0.22	1.93	35.7	8.0	4.20
Allochthonous breccia	0.24	0.87	2.50	7.02	0.03	0.39	49.7	0.11	1.66	37.4	30.0	4.8

The samples are from the main outcrop (point 7).
[a]Limestone fragment from the autochthonous breccias.
[b]Loss on ignition.

DISCUSSION

Geology and Geochemistry of Impactites

The discovery of an impact structure within the Agoudal iron meteorite strewn field is intriguing, because the crater may correspond to the impact point of the main mass of the meteorite. However, clear interpretation of geological observations of the Agoudal site is difficult due to the shapelessness and highly eroded state of the impact structure. The fractured limestone with shatter cones found in the basement of the main outcrop of the impact structure should represent an autochthonous breccia deposit, while the polymict breccia could represent an allochthonous breccia as defined by Stoeffler and Grieve (2007).

Bulk composition of the allochthonous breccia is mostly similar to that of the target limestones (Table 7). We estimated the abundance of impactor material in the breccias based on Ni contents in the target rocks and breccias (8 and 30 ppm Ni respectively, Table 7) and the Agoudal iron (5.5 wt% Ni, Chennaoui Aoudjehane et al. 2013). Our estimate is 0.04 wt%; however, Ni could be redistributed between the meteorite fragments, breccia and target during weathering of the metal and infiltration of groundwater into the target limestones. It should be noted here that measured abundances of Ni in the Fe oxides and Si-Al inclusions in the matrix of the breccia are below the detection limit of the microprobe analyses (Table 4). Based on these reasons, the calculated estimate does not correspond to the real, much lower than 0.04 wt% abundance of meteorite material dispersed in the breccias, which generally suggest insignificant contamination of the breccia by impactor material.

Shatter cones are very important shock indicators (Dietz 1960), and their presence is generally regarded as a tool for recognition of impact structures (e.g., French 1998). The shock pressure required for their formation is in the range of 2–10 GPa (French 1998). The quartz grains occurring in the breccias and target rocks of the impact structure found inside the Agoudal strewn field mostly do not demonstrate any PDF, which form at shock pressure ≥5 GPa (Stöffler and Langenhorst 1994; French 1998). Two quartz grains observed in thin section have only one set of nondecorated PDF per grain, and, if they are true PDF, this would only slightly expand the range of possible shock pressure for Agoudal impact up to 5–10 GPa (Stöffler and Langenhorst 1994).

Rare polymineral clast-bearing Si-Al-rich inclusions observed in the allochthonous breccias have fluidal textures, contain gas-filled bubbles, and are different in composition from the lithologies dominating in the

breccias. These could represent weathered relics of devitrified impact glasses resulting from only local, small-scale shock melting and followed by quick cooling. If this suggestion is plausible, the fluidal textures and compositional variability in the Si-Al inclusions together could be interpreted as a result of an immiscibility of carbonaceous and siliceous melts, which has been observed before at the Haughton, Ries, and Chixulub craters (Martinez et al. 1994; Graup 1999; Jones et al. 2000).

The generally low abundance of the material that could be interpreted as possible products of shock melting in the impact breccias could indicate peak shock pressure up to 30 GPa for the case of a carbonate-rich target (Heider and Kenkmann 2003; Kowitz et al. 2013). Taking into account the highly eroded state of the impact structure, these estimations indicate only the lower limit of the shock pressure; the mineralogical indicators of higher pressures could be removed by erosion.

Genetic Relationship of the Impact Structure and Agoudal Meteorite Shower

The discovery of iron meteorite fragments within the allochthonous impact breccia, with a chemical composition in major and trace siderophile elements similar to that of the Agoudal iron meteorite, suggests a possible syngenetic origin of the impact structure and the Agoudal iron meteorite shower. We also noted that the compositions of the Fe-Ni inclusions in the polymict breccia, and of the Agoudal iron meteorite samples, both plot to lower Ni and Ga or Ge than the main cluster of compositions of IIAB meteorites (Chennaoui Aoudjehane et al. 2013), and closer to the composition of NWA 3201, classified by Wasson et al. (2007) as an IIAB iron (Fig. 9).

Our model calculations show that a meteoroid fall that could form a strewn field similar to the Agoudal strewn field by geometry, total mass of finds, and largest recovered mass (tens to hundreds of kg), could also lead to formation of one or more craters a few tens of m in diameter and produce shock pressures up to approximately 30 Gpa, similar to those estimated for the discovered impact structure. This could be additional support for a potential syngenetic origin of the impact structure and the Agoudal meteorite strewn field.

We cannot exclude the possibility that the Agoudal strewn field by chance overlapped a pre-existing impact structure formed by an impactor of similar composition. Although overlapping meteorite strewn fields have been observed in some regions (e.g., Schlüter et al. 2002), the possibility described above seems to be highly unlikely due to large differences in the rate of small meteorite falls and crater-forming falls. The crater appears to be approximately as old as the Agoudal iron meteorite, but it is difficult to compare the ages of the iron meteorite samples from the Agoudal strewn field and the Agoudal crater without accurate determination of terrestrial ages of the iron meteorites from the strewn field and the Fe-Ni inclusions from the impact breccia, or the age of formation of the melt from the impact breccia.

Reconstruction of the Impact Structure Formation and Ejecta Distribution

In contrast to younger well-documented strewn fields, such as Sikhote-Alin or Campo del Cielo, the Agoudal strewn field and the impact structure are strongly eroded and appear to have been disturbed by human activities. The contact of the allochthonous impact breccias and brecciated target rocks found at the main outcrop marks the level of the pristine floor of the impact structure. The occurrence of limestone fragments with shatter cones, inclusions of meteorite iron and possible traces of small-scale impact melting of the target in the allochthonous breccia could indicate a relative proximity of the outcrop location to the center of the impact structure.

We propose three possible scenarios (small, intermediate, and large) with a hope that future studies may help to narrow this range. According to our models, the smallest meteoroid that allows the simultaneous formation of one small impact structure and the observed strewn field of meteorites has a diameter of 1.4 m entering at angle 60° to horizon. Fragmentation of the meteoroid in the atmosphere produces a largest crater-forming fragment of approximately 460 kg that reaches the surface with a velocity of 3.2 km s^{-1}, plus several smaller (<100 kg) and slower (0.1–0.2 km s^{-1}) fragments. The total calculated final mass in this modeled scenario is slightly above 550 kg; the length of the strewn field is approximately 5 km. The approximately 15 m diameter approximately corresponds to the observed size of the impact site (approximately 30 m). The difficulty of the scenario is that the volume of target rocks loaded up to approximately 5 GPa is rather small in comparison to that of the main impactite outcrop. Moreover, the recent discovery of another two outcrops of shatter cones (Chennaoui Aoudjehane et al. 2014) makes this scenario unlikely. These additional outcrops (Fig. 3c) are located approximately 150 m west (CA1) and approximately 150 m north (CA2) of the main outcrop. They are not covered by allochthonous breccias and are more deeply eroded than the main outcrop. Outcrop CA2 is located at approximately the same absolute

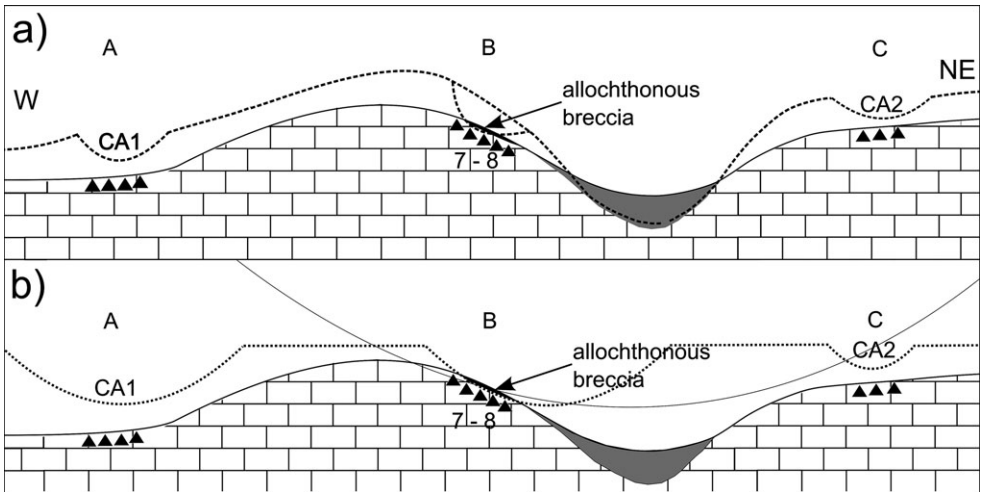

Fig. 11. Schematic cross section of the Agoudal impact site along the line ABC (see Fig. 3c). a) Solid line is a modern relief profile; blocky fill—limestones; gray fill—proluvial sediments in the wadi; triangles—autochthonous breccias; dashed line is a version of pre-erosion surface profile for an inclined target scenario of the multicrater model; b) dotted line—a version of pre-erosion surface profile for a flat horizontal target scenario of the crater field model; thin solid line is a contour of hypothetical large single impact crater.

elevation as the main outcrop, while CA1 is lower, near the bed of the wadi. Assuming that all outcrops with shatter cones are the remnants of a single crater, the crater should be at least 400 m in diameter (Fig. 3c). This scenario is also questionable because in a single large crater the autochthonous breccia with shatter cones should occur throughout the area between the CA1 and CA2 outcrops independently of the erosion state of the impact structure, and this is not the case.

As an alternative to a large crater scenario for the impact sites near Agoudal, we propose a model of a crater field. The different erosion depth of the impactite outcrops could indicate a preimpact irregularity of the surface relief (Fig. 11a). The impact forming the main impactite outcrop occurred on the eastern slope of a wadi (Fig. 11a) or, alternatively, on a pre-existing flat horizontal surface (Fig. 11b). The latter scenario seems to be less likely because it requires a higher denudation rate of the surface of the whole south side of the main valley, which is inconsistent with the preservation of the meteorite strewn field syngenetic to the crater-forming impactor.

The minimum appropriate multicrater model implies a projectile (meteoroid) approximately 3–4 m in diameter fragmented in the atmosphere into a few large and numerous small pieces. In this case, the crater field covers an area approximately 500 m in diameter and consists of a few 10–30 m craters, shrapnel (ejecta from the impact craters), and individual fragments (Figs. 10c and 10d). It is possible that the original Agoudal strewn field was similar to the Sikhote-Alin strewn field, which had 23 craters >9 m and 4 craters >20 m (Krinov 1971). This scenario is also more probable than a large crater scenario from the viewpoint of impact statistics. The absence of numerous craters within the Agoudal strewn field indicates that most of them could have been erased by active denudation processes. Erosion of several closely located craters adjacent to each other could lead to formation of a relatively large area of weakly shocked target rocks similar to that observed at the main impactite outcrop. The weakest point of this scenario is the absence of large-mass meteorite fragments around the remnants of impact craters. More field work could help clarify if such fragments are present but deeply buried or potentially have been previously collected over time.

Ejecta modeling predicts a relatively dense distribution of impactor ejecta near the crater (Figs. 10d and 10e). However, as shown above, the area around the impactite outcrops is poor in meteorite fragments. The impact forming the main impactite outcrop occurred on the eastern slope of a wadi (Fig. 11a). Craters forming on slopes are highly unstable (Elbeshausen et al. 2013); their sides are likely to collapse, filling the crater with fragmented target materials (breccias) and burying impactor fragments to an approximately 5 m depth. Thus, we suggest that shrapnel fragments could have been deeply buried under the sediments in the wadis or have been almost fully collected previously.

The distribution of small finds of the Agoudal iron meteorite mostly to the E-SE from the crater is in agreement with the sloped target scenario. The area of distribution of meteorite fragments ejected from the crater should occupy a significant part of the strewn field

formed during the mid-air fragmentation of the Agoudal iron meteorite. Thus, the northern finds grouping approximately 1.5 km from the impact structure could either be individual fragments (e.g., the 52 kg sample) or shrapnel fragments ejected from the crater. The finds around point 1 are located at approximately the same distance (1.2–1.8 km) from the main outcrop of the impact structure as the northern cluster of finds and some of the samples of indefinite shape could be shrapnel. The southern finds, located at 4.5 km south of the crater, most likely are individual samples.

According to the model calculations, both shocked (with shatter cones) and nonshocked target materials ejected from the crater are distributed over a relatively large area. Fragments of limestone with shatter cones which were found in quaternary deposits approximately 300 m to the south and northeast of the main impactite outcrop (Chennaoui Aoudjehane et al. 2014) correspond to the model distribution of shocked target ejecta. The sporadic distribution of target ejecta finds could be explained by intensive erosion of crater ejecta deposits.

Strewn Field Geometry

The overall scattering area is approximately 10 km^2, though the density of finds and the total collected mass are relatively small in comparison to other similar showers (e.g., Sikhote-Alin). The initial distribution of Agoudal finds by mass has been strongly affected by the undocumented collection of meteorites and/or natural factors such as large terrestrial age, burial of the meteorites in alluvium, intensive erosion, and complex relief. Overlaying the shrapnel and individual fragment strewn fields complicates the situation further, making the orientation of the fall trajectory uncertain. Some key points for reconstruction of the scattering area's orientation are the individual sample (52 kg, Table 2) found in the northern valley, finds of small individual samples around point 1, the southern cluster of finds, and the relics of the impact structure, which is potentially syngenetic to the Agoudal meteorite. Lines drawn through the relics of the impact structure and the northern and southern clusters (Fig. 2) correspond to a range of possible orientations of the strewn field axis, which is approximately SE–NW. The area east of point 1 has not been searched, so it is not known if the strewn field continues further in that direction. The strewn field is at least 6 km long by 2 km wide.

Unique Formation Settings of the Impact Structure Found Near Agoudal

Field observations and the results of model calculations have shown that the found relic impactites—shatter cones and breccias—could have resulted from the impact of several approximately 500 kg fragments of the meteoroid forming the Agoudal meteorite strewn field. The proposed crater field comprises several craters less than 150 m in diameter in which well-developed fine-textured shatter cones have been formed and preserved due to a number of favorable conditions (thin soil layer, consolidated sedimentary target, and appropriate parameters of the projectile). This unique discovery for Earth (Table 1) offers an intriguing comparison to Mars, where sedimentary rocks occur (e.g., McLennan et al. 2014), the observed present-day, small-scale impact cratering rate is higher than on Earth (e.g., Daubar et al. 2013), and the modern erosion rate is lower due to Mars' dry current environment. Thus, the formation of the Agoudal impact structure may be used as a prototype for the future investigation of rocks inside and around small Martian craters.

CONCLUSIONS

The Agoudal iron meteorite strewn field is a unique site in Morocco where the relics of several possible impact structures have been discovered. These relics are the first confirmed impact site in Morocco and appear to be related to the Agoudal meteorite. The initial distribution of meteorite fragments within the Agoudal strewn field cannot be unambiguously reconstructed due to natural factors and previous undocumented collection of meteorite material. The total estimated collected mass of the Agoudal iron is approximately 500 kg. The estimation of strewn field size is at least 6 × 2 km; approximate orientation of the strewn field axis is SE–NW. The most likely formation scenario includes a projectile 3–4 m in diameter creating a field of a few 10–20 m diameter craters downrange of a strewn field of small low-velocity meteorite fragments released after fragmentation during the incoming trajectory. Peak shock pressures during crater formation could be as high as 30 GPa with most target rocks loaded below 5 GPa. Potentially, the largest fragments of the meteorite may be deeply buried and could be detected by geophysical search techniques. The relics of the impact structures found near the Agoudal strewn field represent typological examples of small impact craters in a consolidated sediment target formed on sloping terrain, similar to small crater fields on Mars.

Acknowledgments—This work was supported by the Dedovsk Museum of the History of the Universe (DMUH). N. Artemieva was supported by RFBR grant 13-05-00309_a. H. Chennaoui Aoudjehane was supported by Barringer Crater company, the program CMIFMP Volubilis (MA/11/252), and CNRST-Morocco

and CNRS-France, PICS (SDU 01/10). M. Humayun acknowledges support from the NASA Cosmochemistry program (NNX13AI06G). We thank Ya. V. Bychkova (Institute of Geology of Ore Deposits, Petrography, Mineralogy and Geochemistry, Moscow, Russia [IGEM RAS]) for help and assistance in providing of ICP-MS analyses. We thank Dr. Michael Poelchau, Dr. Luigi Folco, and Prof. A. J. Timothy Jull for their scientific reviews that helped to improve this manuscript. We are also grateful to Brennan Klose for careful linguistic editing.

Editorial Handling—Dr. A. J. Timothy Jull

REFERENCES

Artemieva N. A. and Shuvalov V. V. 2001. Motion of a fragmented meteoroid through the planetary atmosphere. *Journal of Geophysical Research* 106:3297–3310.

Bevan A. W. R., Shoemaker E. M., and Shoemaker C. S. 1995. Metallography and thermo mechanical treatment of the Veevers (IIAB) crater-forming iron meteorite. *Records of the Western Australian Museum* 17:51–59.

Bland P. A. and Artemieva N. A. 2006. The rate of small impacts on Earth. *Meteoritics & Planetary Science* 41:607–631.

Bunch T. E. and Cohen A. J. 1964. Shock deformation of quartz from two meteorite craters. *Geological Society of America Bulletin* 75:1263–1266.

Campbell A. J., Humayun M., and Weisberg M. K. 2002. Siderophile element constraints on the formation of metal in the metal-rich chondrites Bencubbin, Weatherford, and Gujba. *Geochimica et Cosmochimica Acta* 66:647–660.

Cassidy W. A., Villar L. M., Bunch T. E., Kohman T. P., and Milton D. J. 1965. Meteorites and craters of Campo del Cielo, Argentina. *Science* 149:1055–1064.

Chao E. C. T., Fahey J. J., and Littler J. 1961. Coesite from Wabar Crater, near Al Hadida, Arabia. *Science* 133:882–883.

Chennaoui Aoudjehane H., Garvie L. A. J., Herd C. D. K., Chen G., and Aboulahris M. 2013. Agoudal: the most recent iron meteorite from Morocco (abstract #5025). 76th the Annual Meteoritical Society Meeting.

Chennaoui Aoudjehane H., Reimold W. U., Koeberl C., Bouley S., Aoudjehane M., Aboulahris M., El Kerni H., Hutzler A., Bourles D., and Rochette P. 2014. Agoudal (High Atlas Mountains): Confirmation of remnants of a post mid-Jurassic impact structure in Morocco. 45th Lunar and Planetary Science Conference. LPI Contribution 1777. Houston, Texas: Lunar and Planetary Institute. 2053 p.

Classen J. 1978. The Meteorite Craters of Morasko in Poland. *Meteoritics* 13:245.

Daubar I. J., McEwen A. S., Byrne S., Kennedy M. R., and Ivanov B. 2013. The current martian cratering rate. *Icarus* 225:506–516.

Dietz R. S. 1960. Meteorite impact suggested by shatter cones in rock. *Science* 131:1781–1784.

Dominik B. 1977. Shock and thermal transformations in meteorites from the Morasko craterfield. *Meteoritics* 12:207.

D'Orazio M., Folco L., Zeoli A., and Cordier C. 2011. Gebel Kamil: The iron meteorite that formed the Kamil crater (Egypt). *Meteoritics & Planetary Science* 46:1179–1196.

Earth Impact Database. 2011. http://www.passc.net/EarthImpactDatabase/. Accessed November 20, 2014.

Elbeshausen D., Krohn K., Wünnemann K., Jaumann R., Russell C. T., and Raymond C. A. 2013. Bimodal craters on Vesta: Impacts on slopes studied by numerical simulations. 44th Lunar and Planetary Science Conference. LPI Contribution No. 1719, p.1903.

Ellero A., Ottria G., Malusà M. G., and Ouanaimi H. 2012. Structural geological analysis of the High Atlas (Morocco): Evidences of a transpressional fold-thrust belt. In *Tectonics–recent advances*, edited by Sharkov E. Rijeka, Croatia: InTech. pp. 229–258. doi:10.5772/50071.

Folco L. and D'Orazio M. 2011. Shocked quartz at the Kamil crater (Egypt) (abstract 5018). 74th Annual Meeting of the Meteoritical Society. *Meteoritics & Planetary Science Supplement* 46:A67.

Folco L., Di Martino M., El Barkooky A., D'Orazio M., Lethy A., Urbini S., Nicolosi I., Hafez M., Cordier C., van Ginneken M., Zeoli A., Radwan A. M., El Khrepy S., El Gabry M., Gomaa M., Barakat A. A., Serra R., and El Sharkawi M. 2010. The Kamil Crater in Egypt. *Science* 329:804.

Folco L., Di Martino M., El Barkooky A., D'Orazio M., Lethy A., Urbini S., Nicolosi I., Hafez M., Cordier C., van Ginneken M., Zeoli A., Radwan A. M., El Khrepy S., El Gabry M., Gomaa M., Barakat A. A., Serra R., and El Sharkawi M. 2011. Kamil crater (Egypt): Ground truth for small-scale meteorite impacts on Earth. *Geology* 39:179–182.

French B. M. 1998. Traces of catastrophe: A handbook of shock-metamorphic effects terrestrial meteorite impact structures. Technical Report, LPI Contribution 954. Houston, Texas: Lunar and Planetary Institute. 120 p.

Graup G. 1999. Carbonate-silicate liquid immiscibility upon impact melting, Ries Crater, Germany. *Meteoritics & Planetary Science* 34:425–438.

Heider N. and Kenkmann T. 2003. Numerical simulation of temperature effects at fissures due to shock loading. *Meteoritics & Planetary Science* 38:1451–1460.

Holsapple K. A. and Housen K. R. 2007. A crater and its ejecta: An interpretation of Deep Impact. *Icarus* 187:345–356.

Humayun M. 2012. Chondrule cooling rates inferred from diffusive profiles in metal lumps from the Acfer 097 CR2 chondrite. *Meteoritics & Planetary Science* 47:1191–1208.

Humayun M., Simon S. B., and Grossman L. 2007. Tungsten and hafnium distribution in calcium-aluminum inclusions (CAIs) from Allende and Efremovka. *Geochimica et Cosmochimica Acta* 71:4609–4627.

Johnson P. H., Bogard D. D., and Hoerz F. 1988. Shock-implanted noble gases in samples from the Wabar impact crater: Implications for other terrestrial craters and the surface of Mars (abstract). 19th Lunar and Planetary Science Conference. p. 557.

Jones A. P., Claeys P., and Heuschkel S. 2000. Impact melting of carbonates from the Chicxulub crater. In *Impacts and the early earth. Lecture notes in earth sciences*, edited by Gilmour I. and Koeberl C. Berlin: Springer Verlag. pp. 343–362.

Kenkmann T., Artemieva N. A., Wünnemann K., Poelchau M. H., Elbeshausen D., and Núñez Del Prado H. 2009.

The Carancas meteorite impact crater, Peru: Geologic surveying and modeling of crater formation and atmospheric passage. *Meteoritics & Planetary Science* 44:985–1000.

Kofman R. S., Herd C. D. K., and Froese D. G. 2010. The Whitecourt meteorite impact crater, Alberta, Canada. *Meteoritics & Planetary Science* 45:1429–1445.

Kowitz A., Güldemeister N., Reimold W. U., Schmitt R. T., and Wünnemann K. 2013. Diaplectic quartz glass and SiO_2 melt experimentally generated at only 5 GPa shock pressure: laboratory observations versus mesoscale modeling (abstract #1461). 44th Lunar and Planetary Science Conference. CD-ROM.

Krinov E. L. 1971. New studies of the Sikhote-Alin iron meteorite shower. *Meteoritics* 6:127–138.

Martinez I., Agrinier P., Schärer U., and Javoy M. 1994. A SEM-ATEM and stable isotope study of carbonates from the Haughton impact crater, Canada. *Earth and Planetary Science Letters* 121:559–574.

McLennan S. M., Anderson R. B., Bell J. F. III, Bridges J. C., Calef F. III, Campbell J. L., Clark B. C., Clegg S., Conrad P., Cousin A., Des Marais D. J., Dromart G., Dyar M. D., Edgar L. A., Ehlmann B. L., Fabre C., Forni1 O., Gasnault O., Gellert R., Gordon S., Grant J. A., Grotzinger J. P., Gupta S., Herkenhoff K. E., Hurowitz J. A., King P. L., Le Mouélic S., Leshin L. A., Léveillé R., Lewis K. W., Mangold N., Maurice S., Ming D. W., Morris R. V., Nachon M., Newsom H. E., Ollila A. M., Perrett G. M., Rice M. S., Schmidt M. E., Schwenzer S. P., Stack K., Stolper E. M., Sumner D. Y., Treiman A. H., VanBommel S., Vaniman D. T., Vasavada A., Wiens R. C., Yingst R. A., and MSL Science Team. 2014. Elemental geochemistry of sedimentary rocks at Yellowknife Bay, Gale crater, Mars. *Science* 343:1244734. doi:10.1126/science.1244734.

Melosh H. J. 1989. *Impact cratering: A geologic process. Oxford monographs on geology and geophysics*. Oxford: Oxford University Press. 245 p.

Michard A., Ibouh H., and Charriere A. 2011. Syncline-topped anticlinal ridges (STARs) from the High Atlas: A Moroccan conundrum, and inspiring structures from the Syrian Arc, Israel. *Terra Nova* 23:314–323.

Nininger H. H. 1963. Meteorite distribution on the Earth. In *The moon, meteorites and comets*, edited by Gerard P. K. and Middlehurts B. Chicago, Illinois: The University of Chicago Press. 162 p.

Nininger H. H. and Figgins J. D. 1933. The excavation of a meteorite crater near Haviland, Kiowa County, Kansas. *American Journal of Science* 28:312–313.

Plado J. 2012. Meteorite impact craters and possibly impact-related structures in Estonia. *Meteoritics & Planetary Science* 47:1590–1605.

Poelchau M. H., Kenkmann T., Thoma K., Hoerth T., Dufresne A., and Schäfer F. 2013. The MEMIN research unit: Scaling impact cratering experiments in porous sandstones. *Meteoritics & Planetary Science* 48:8–22.

ReVelle D. O. and Ceplecha Z. 1994. Analysis of identified iron meteoroids: Possible relation with M-type Earth-crossing asteroids? *Astronomy & Astrophysics* 292:330–336.

ReVelle D. O. and Rajan R. S. 1988. Identification of nickel-iron material among the prairie network fireballs. *Bulletin of the American Astronomical Society* 20:862.

Sadilenko D. A., Lorenz C. A., Ivanova M. A., Roshchina I. A., and Korochantsev A. V. 2013. A new small impact crater in the High Atlas, in the Agoudal iron strewn field (abstract #5215). 76th Annual Meteoritical Society Meeting. Meteoritics and Planetary Science Supplement.

Schlüter J., Schultz L., Thiedig F., Al-Mahdi B. O., and Abu Aghreb A. E. 2002. The Dar al Gani meteorite field (Libian Sahara): Geological setting, pairing of meteorites and recovery density. *Meteoritics & Planetary Science* 37:1079–1093.

Semenenko V. P., Samoilovich L. G., and Kozlov I. S. 1982. Signs of shock metamorphism in the Kaali meteorite (In Russian). *Meteoritika* 41:96–100.

Shoemaker E. M. 1977. Astronomically observable crater-forming projectiles. In *Impact and explosion cratering*, edited by Roddy D. J., Pepin R. O., and Merrill R. B. New York: Pergamon Press. pp. 617–628.

Shoemaker E. M., MacDonald F. A., and Shoemaker C. S. 2005. Geology of five small Australian impact craters. *Australian Journal of Earth Sciences* 52:529–544.

Shuvalov V. V. 1999. 3D hydrodynamic code SOVA for interfacial flows, application to the thermal layer effect. *Shock Waves* 9:381–390.

Shuvalov V. V. 2002. Displacement of target material due to impacts (abstract #1259). 33rd Lunar and Planetary Science Conference. CD-ROM.

Spencer L. J. 1933. Meteoric iron and silica-glass from the meteorite craters of Henbury (central Australia) and Wabar (Arabia). *Mineralogical Magazine and Journal of Mineralogical Society* 42:387–404.

Stöffler D. and Langenhorst F. 1994. Shock metamorphism of quartz in nature and experiment: I. Basic observation and theory. *Meteoritics & Planetary Science* 29:155–181.

Stoeffler D. and Grieve R. A. F. 2007. Impactites. In *Metamorphic rocks: A classification and glossary of terms, Recommendations of the International Union of Geological Sciences*, edited by Fettes D. and Desmons J. Cambridge, UK: Cambridge University Press. pp. 82–92.

Trunin R. F., Gudarenko L. F., Zhernokletov M. V., and Simakov G. V. 2001. *Experimental data on shock compression and adiabatic expansion of condensed matter*. Sarov: Russian Federal Nuclear Center-VNIIEF. 446 p.

Wasson J. T., Ouyang X., Wang J., and Jerde E. 1989. Chemical classification of iron meteorites. XI - Multi-element studies of 38 new irons and the high abundance of ungrouped irons from Antarctica. *Geochimica et Cosmochimica Acta* 53:735–744.

Wasson J. T., Huber H., and Malvin D. J. 2007. Formation of IIAB iron meteorites. *Geochimica et Cosmochimica Acta* 71:760–781.

Zotkin I. T. and Tsvetkov V. 1983. On the form of iron meteoroids. *Solar System Research* 17:60–62.